PLANT SCIENCES

Time-resolved tracking of cellulose biosynthesis and assembly during cell wall regeneration in live *Arabidopsis* protoplasts

Hyun Huh[1]†, Dharanidaran Jayachandran[2]‡, Junhong Sun[3]§, Mohammad Irfan[2]¶, Eric Lam[3]*, Shishir P. S. Chundawat[2]*, Sang-Hyuk Lee[1,4]*

Cellulose, the most abundant polysaccharide on earth composing plant cell walls, is synthesized by coordinated action of multiple enzymes in cellulose synthase complexes embedded within the plasma membrane. Multiple chains of cellulose fibrils form intertwined extracellular matrix networks. It remains largely unknown how newly synthesized cellulose is assembled into an intricate fibril network on cell surfaces. Here, we have established an in vivo time-resolved imaging platform to continuously visualize cellulose biosynthesis and fibril network assembly on *Arabidopsis thaliana* protoplast surfaces as the primary cell wall regenerates. Our observations provide the basis for a model of cellulose fibril network development in protoplasts driven by an interplay of multiscale dynamics that includes rapid diffusion and coalescence of nascent cellulose fibrils, processive elongation of single fibrils, and cellulose fibrillar network rearrangement during maturation. This study provides fresh insights into the dynamic and mechanistic aspects of cell wall synthesis at the single-cell level.

INTRODUCTION

Plant cell walls are complex extracellular matrices, which are predominantly composed of sink polysaccharides in the form of semicrystalline cellulose microfibrils (CMFs) intertwined with amorphous matrix polysaccharides such as hemicellulose and pectin. They can be largely classified into primary and secondary cell walls that are assembled at different developmental stages with varying compositions and ultrastructural organizations of associated polysaccharides (*1*). The thinner and more extensible primary cell wall can better facilitate the continuous expansion of plant cells during growth and development. In contrast, the thicker secondary cell wall is more rigid and provides structural strength to plant cells and tissues (*2*). The primary cell wall, which is formed early in cell division and expansion, dictates the cell shape and acts as a template for the secondary cell wall deposition (*3*). The primary cell wall has been studied for a long time with particular emphasis on cellulose, which has been shown to form intricate fibrillar networks (*4*, *5*). Cellulose, a linear β-1,4-glucan homopolymer chain, is synthesized by the plasma membrane–embedded glycosyltransferase enzyme family called cellulose synthase (CESA) that exists in various isoforms (*6*, *7*). CESAs self-assemble into a supramolecular protein complex called cellulose synthase complex (CSC) (*8*, *9*). Multiple cellulose chains are synthesized by a single CSC in a coordinated fashion involving extrusion out of the cell membrane to eventually form bundles of semicrystalline cellulose fibrils, referred to as "elementary fibrils," the smallest biological structural unit of cellulose (*4*, *10*). Furthermore, multiple elementary fibrils can bundle into thicker fibrils, known as "CMFs" (*4*, *10*, *11*).

Cell wall structure has been extensively studied by microscopy since Hooke (*12*) had described, for the first time, the boxlike cell walls of cork wood and other plants under his microscope as "cells" because they reminded him of cells in a monastery. More recently, electron microscopy (EM) has been used early on to visualize and study the structure of the fibrillar cell wall polysaccharides at higher resolution during plant cell development (*13*, *14*). Atomic force microscopy (AFM) has also been widely used for studies of cell walls, because of its compatibility with imaging hydrated samples and minimal sample preparation requirements, contributing substantially to our understanding of plant cell wall structure (*4*, *10*, *15*–*19*). Both high-resolution microscopy techniques (i.e., EM and AFM), while providing sharp nanoscale images, lack molecular specificity and are incompatible with live-cell imaging (*4*, *13*, *14*, *18*). Fluorescence microscopy has great advantages over other imaging methods in this regard, making it an important tool for visualizing distinct cell wall components. Plant cell wall–binding chemical dyes such as Calcofluor white (CFW), Congo red, and Pontamine Fast Scarlet 4BS (PFS) are commonly used to stain cellulose in plant cell walls for fluorescence microscopy (*20*–*23*). However, most organic dyes bind nonspecifically to polysaccharides other than cellulose, may alter cellulose crystallinity in vivo, and can be toxic to living cells (*24*–*26*). In contrast, carbohydrate-binding modules (CBMs) are noncatalytic protein domains associated with the glycosyl hydrolases that bind to cell wall polysaccharides in a target-specific manner: CBM3a for crystalline cellulose (*27*, *28*); CBM17 and CBM28 for amorphous cellulose (*28*, *29*); CBM76 for xyloglucan (*30*); and CBM27 for mannans (*31*). CBMs have been used to label various cell wall polysaccharides via conjugation with fluorescent proteins (*15*, *32*, *33*) or chemical dyes (*34*–*36*). Such fluorescent probes can be imaged with widefield epifluorescence or scanning laser confocal

[1]Institute for Quantitative Biomedicine, Rutgers University, 174 Frelinghuysen Rd, Piscataway, NJ 08854, USA. [2]Department of Chemical and Biochemical Engineering, Rutgers University, 98 Brett Rd, Piscataway, NJ 08854, USA. [3]Department of Plant Biology, Rutgers University, 59 Dudley Rd, New Brunswick, NJ 08901, USA. [4]Department of Physics and Astronomy, Rutgers University, 136 Frelinghuysen Rd, Piscataway, NJ 08854, USA.
*Corresponding author. Email: shishir.chundawat@rutgers.edu (S.P.S.C.); eric.lam@rutgers.edu (E.L.); shlee@physics.rutgers.edu (S.-H.L.)
†Present address: Hackensack Meridian Health Center for Discovery and Innovation, 111 Ideation Way, Nutley, NJ 07110, USA.
‡Present address: Buckman Laboratories International Inc., 1256 North McLean Blvd, Memphis, TN 38108, USA.
§Present address: Waksman Institute of Microbiology, Rutgers University, 190 Frelinghuysen Rd, Piscataway, NJ 08854, USA.
¶Present address: Plant Biology Section, School of Integrative Plant Science, Cornell University, 236 Mann Dr, Ithaca, NY 14853, USA.

microscopy, but the diffraction-limited optical resolution often proves insufficient to resolve nanoscale fibril ultrastructures of cell wall polysaccharides. This diffraction barrier can be overcome with super-resolution fluorescence microscopy techniques (*37*–*40*), and such approaches have been applied to plants in recent decades (*23*, *41*–*45*). However, application of super-resolution fluorescence imaging techniques to visualize cell wall polysaccharides is still in its early stages (*23*, *44*, *45*).

While we have a relatively good understanding of the mature plant cell wall structure, the dynamic processes by which polysaccharides are synthesized and assembled into fibrillar structures of distinct architectures within cell walls remain largely unknown. Real-time imaging of live plant tissues or cells with time-lapse microscopy is critical to bridge the knowledge gaps in our understanding of the mechanisms involved to construct a cell wall on the plant cell surface. In this respect, transgenic plants expressing CESA fusion to fluorescent protein have been used to visualize and track CESA/CSC motility in living plant tissues, and it has been shown that CESAs/CSCs move linearly at a speed of ~0.2 to 0.4 μm/min, with their localization and motion guided by cortical microtubules and/or preexisting CMFs (*46*–*49*). CESA enzyme (or CSC) motion observed in such studies was presumed to be tightly coupled with cellulose synthesis, but direct high-resolution visualization of nascent cellulose fibril growth in plant tissues or isolated plant cells has not been reported yet, although cellulose fibril motion was captured in the context of reorientation during cell wall expansion (*22*), conformational change under tension (*50*), and degradation by hydrolytic enzymes (*18*). The polylamellate structure of plant cell wall is typically composed of ~100 lamellae, with CMFs forming a fine reticulated network on each lamellar surface (*4*, *13*). Expectedly, it is very challenging to separately visualize only the growing nascent cellulose fibrils amid the background of underlying multilayered cellulose network on the surface of intact plant tissues. In that regard, plant protoplasts that could regenerate cell walls have tremendous potential to be used as a model system to study cell wall synthesis in vivo. Confocal microscopy has been used for three-dimensional (3D) imaging of protoplasts (*51*–*53*), and even time-lapse imaging of cell wall regeneration was attempted for *Physcomitrella patens* protoplasts albeit at low resolution (*54*). However, traditional confocal microscopy techniques have not proven suitable for long-term live-cell imaging of plant protoplasts owing to phototoxicity (*55*, *56*). Furthermore, all previous protoplasts cell wall regeneration microscopy studies have used chemical dyes such as CFW and PFS to stain cellulose, which are not ideal for longer-duration, noninvasive, live-cell microscopy imaging that can lasts over several hours to days. Such limitations combined with the fragile nature of protoplasts, which makes them highly susceptible to damage by environmental/imaging conditions, have posed substantial challenges for imaging the dynamic process of plant cell wall regeneration in real time.

In this work, we have succeeded to image cellulose biosynthesis and its assembly into CMF during the entire process of cell wall regeneration for *Arabidopsis* protoplasts and studied the processes through which intertwined cellulose fibril networks develop at the single-cell level with high spatiotemporal resolution. To achieve this, we established an in vivo plant cell imaging platform based on total internal reflection fluorescence microscopy (TIRFM), in situ cellulose fluorescence labeling with fluorophore-conjugated tandem carbohydrate binding modules (tdCBM), and tight control of temperature and lighting conditions best suited for plant protoplast cell wall regeneration. We discovered that cellulose fibrillar networks on plant protoplast cell surfaces develop in multiple stages, and our observations provide fresh insights into how cell walls are made in plants, which has important implications for developing transgenic crops that are optimized for cellulosic bioenergy and agricultural food/feed production.

RESULTS

Visualizing cell wall regeneration in live protoplasts of *Arabidopsis*

Mesophyll protoplasts were isolated from leaves of 3- to 4-week-old *Arabidopsis* Col-0 plants (Fig. 1A). We used medium-sized leaves, because they produced monodispersed protoplasts versus smaller- or larger-sized leaves. Upon incubation in a suitable plant protoplast cell wall regeneration media (WI/M2) under ambient white light provided by a light-emitting diode (LED) bulb (Hue, Philips), protoplasts were biologically active and consistently regenerated cell walls for more than 18 hours. They could be readily visualized by fluorescence microscopy using conventional CFW staining (fig. S1 and Materials and Methods). The experimental workflow is summarized in Fig. 1A.

CFW, although commonly used, is not optimal for visualizing cellulose in live cells because of its nonspecific binding to various plant glycan epitopes and known cell toxicity (*24*–*26*). CBM-based proteinaceous probes were previously developed as a versatile, inert, and target-specific cell wall polysaccharide probe for enabling live-cell imaging as well as other immunolabeling applications (*15*, *27*–*36*). In recent work, we developed a collection of engineered CBMs that were extensively characterized by various biochemical and kinetic analyses to identify CBM-based binding probes that were suitable for live-cell imaging (*57*). Unlike conventional green fluorescent protein (GFP)–CBM3a, tandem CBM3a (tdCBM3a) probes showed minimal protein aggregation in solution and gave reversible binding toward both crystalline and amorphous forms of cellulose. Reversible binding to nascently synthesized cellulose is critical to minimize potential interference with the cell wall regeneration process. Furthermore, we found that GFP was much dimmer at pH 5.5 of the cell wall regeneration media which greatly reduced our signal-to-noise sensitivity to visualize nascently synthesized cellulose fibrils. Therefore, we tethered tdCBM3a with an organic fluorophore dye (Alexa Fluor) that had much higher stability and brightness suitable for our long-term time-lapse and super-resolution fluorescence microscopy experiments. Also, since the size of organic fluorophores is smaller than GFP, this helps minimize potential steric hindrance during CBM-cellulose binding interactions. In summary, we found tdCBM3a to be the most optimal CBM probe for imaging cellulose on *Arabidopsis* protoplast surfaces immersed in cell wall regeneration media and further labeled it with Alexa Fluor 568 dye for long-term imaging with low autofluorescence under our experimental conditions (Materials and Methods). Using low concentrations of Alexa568-tdCBM3a (e.g., 100 nM) added to the cell wall regeneration media, we were able to continually label and image newly synthesized cellulose fibrils on the protoplast surface in situ while maintaining high cell viability and low background fluorescence from unbound dyes over long incubation times. Protoplasts could develop dense CMF networks after 24-hour cell wall regeneration under our experimental conditions (Fig. 1, B and C) and showed no qualitative difference in the CMF architecture produced either in

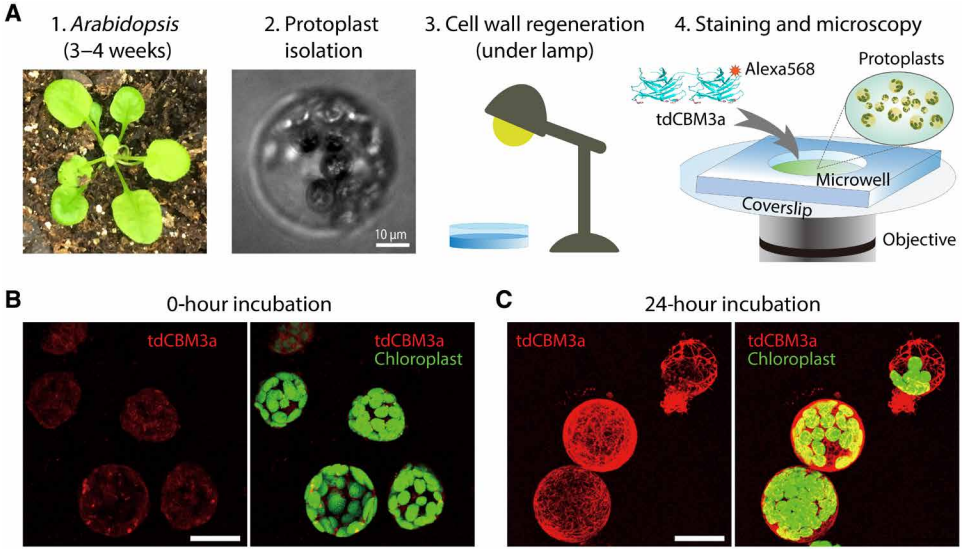

Fig. 1. Workflow for imaging plant protoplast cell wall regeneration. (**A**) Summary of experimental workflow for imaging cellulose biosynthesis in protoplasts. *Arabidopsis* protoplasts were isolated from leaves of 3- to 4-week-old plants by removing existing cell walls using enzymes and were incubated in a suitable cell wall growth media under a white light LED lamp. Fixed or live samples were stained with Alexa568-tdCBM3a to image regenerated cellulose fibrils formed on the protoplast cell surface. (**B** and **C**) Representative 3D confocal fluorescence micrographs of whole protoplasts with cellulose fibrils (red, pseudo-colored) and chloroplasts (green, pseudo-colored) visualized by Alexa568-tdCBM3a (excitation: 561 nm/emission: 590 to 615 nm) and autofluorescence (excitation: 488 nm/emission: 660 to 690 nm), respectively. Here, (B) shows images of cells before incubation with regeneration media, and (C) shows cells after 24-hour incubation in cell wall regeneration media. Scale bars, 10 µm (A) and 20 µm [(B) and (C)].

the presence or absence of the CBM probe (*57*). However, while live-cell time-lapse imaging cannot be achieved without addition of a fluorescent cellulose-binding label (e.g., tdCBM, S4B, or Calcofluor), there could exist potential impacts of any such labeling strategies on the cellular machinery as well as the cellulose fibril assembly dynamics that might not be readily resolved by fluorescence microscopy data alone.

Cellulose is a major polysaccharide of regenerated cell walls

While the Alexa568-tdCBM3a probe was anticipated to bind predominantly to cellulose (*27*, *28*), we further investigated whether the regenerated cell wall morphology visualized by the probe represented cellulose networks by using cellulose enzymatic hydrolysis assays, glycome immunolabeling, and cell wall chemical composition analysis.

Protoplasts with regenerated cell walls were fixed with glutaraldehyde to preserve cell wall integrity and arrest cell wall development after 24 hours. Cells were then labeled with Alexa568-tdCBM3a for visualizing the regenerated CMF network. When fixed protoplasts were subject to hydrolysis with cellulase cocktail (Cellic CTec2, Novozymes) (*58*), we observed complete disappearance of fibrillar structures of the regenerated cell walls within 40 min (Fig. 2A and movie S1). Although this result documented that cellulose was present within the fibrillar structures, comprising the visualized fibril network pattern, we could not exclude the possibility that we were detecting loss of xyloglucan labeled with tdCBM3a (*59*) instead of cellulose. (Note: CTec2 cellulase cocktail is known to contain endoglucanases capable of hydrolyzing xyloglucan and cellulose). To examine this possibility, we immunolabeled xyloglucan with xyloglucan-specific antibody (LM15) that was conjugated with anti-rat immunoglobulin G (IgG) Alexa Fluor 488 secondary antibody (*60*, *61*). Two-color confocal microscopy with Alexa568-tdCBM3a and Alexa488-LM15 showed almost identical regenerated protoplast cell wall morphology in the two fluorescence channels (Fig. 2B). However, when a purified cellulose-specific hydrolytic enzyme (E-CELBA, Megazyme) with no detectable activity toward xyloglucan was added, Alexa568-tdCBM3a fluorescence completely vanished, whereas Alexa488-LM15 fluorescence still remained. The Alexa488-LM15 fluorescence signal in the presence of E-CELBA lost the fibril network pattern and instead was more homogeneously distributed over the cell surface (Fig. 2B). Together, these results strongly suggest the cellulose fibril-specific binding capacity of tdCBM3a and the potential for close association between cellulose fibrils and xyloglucan—the major hemicellulose of plant primary cell walls—to be present on regenerated protoplast cell wall surfaces (*62*).

We next performed acid hydrolysis followed by gas chromatography–mass spectrometry (GC-MS) on plant protoplasts with regenerated cell walls to determine the general monosaccharide composition of matrix polysaccharides (Fig. 2C). Protoplasts with cell walls regenerated for 24 hours in a suitable regeneration media (WI/M2) showed ~4.5-fold increase in the amount of glucose containing polysaccharides as compared to protoplasts lacking cell walls (incubated in W5 media as control). Sugar composition was estimated via GC-MS analysis subsequently to acid hydrolysis of the polysaccharides into their respective monosaccharides, and therefore, the glucan content reported here could have been partially derived from both amorphous cellulose (β-1,4-glucan) and callose (β-1,3-glucan). During the initial stages of cell wall regeneration, callose is known to interact with cellulose to provide stiffness and support (*63*, *64*). However, callose is mainly found in pollen tubes, plasmodesmata, and wounded cells, whereas cellulose is the most abundant structural polysaccharide constituting 30 to 90% of plant cell walls (*65*). We noted that our protoplasts had mostly fibril-shaped fluorescent

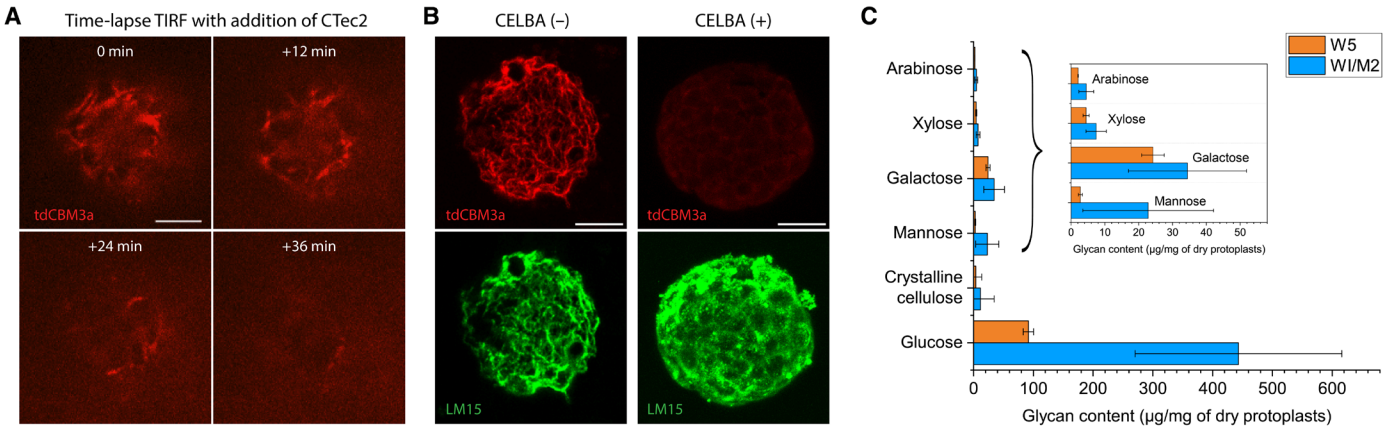

Fig. 2. Identification of cellulose on regenerating protoplast cell membrane surfaces. (**A**) Time-lapse TIRFM images of a protoplast cell surface with its regenerated cell wall fibrillar network being continuously degraded by a commercial cellulase (Cellic CTec2, Novozymes). The fibrillar network on the cell was stained with Alexa568-tdCBM3a. The initial time point (0 min) represents the time at which the CTec2 cellulase was added. (**B**) Two-color confocal images of regenerated protoplasts cell walls and fibrillar network that were labeled with Alexa568-CBM3a (red, pseudo-colored) and Alexa488-LM15 (green, pseudo-colored) to visualize cellulose and xyloglucan, respectively. Left: Cell surface showed patterns of fibril network that were colocalized between the two labels. Right: Addition of cellulose-specific hydrolytic enzyme (E-CELBA) had Alexa568 fluorescence signal completely disappear for all observed protoplasts, whereas the Alexa488 fluorescence remained strong even after the fibril network pattern disappeared. (**C**) Gas chromatography–mass spectrometry (GC-MS) analysis of monosaccharides released after acid hydrolysis of protoplast samples to analyze the chemical composition of cell wall polysaccharides that were produced after incubating protoplasts for 24 hours in the regeneration media (WI/M2) in comparison to the control media (W5). Inset: Magnified view of arabinose, xylose, mannose, and galactose data. Data are represented as mean and SD values that are obtained from $n = 3$ technical replicates. Scale bars, 5 μm (A) and 10 μm (B).

signals after cell wall regeneration, which further helps distinguish cellulose morphology from callose (dot-shaped) based on the shape of the fluorescence image, as also reported previously (*51*). It is also unlikely that tdCBM and purified cellulases would have any binding or catalytic activity toward other glucan polysaccharides like starch. Therefore, in light of the fibril morphology, cellulase activity, and tdCBM binding specificity results, the large amount of glucan polysaccharide observed during GC-MS is likely indicative of cellulose as the major polysaccharide component in regenerated cell walls. In addition, other minor polysaccharides composed of other types of monomer sugars such as galactose, mannose, or xylose were also detected and showed slightly increased amount in the protoplasts with regenerated cell walls although in much lower absolute amounts than glucan polymers (Fig. 2C, inset).

Crystalline cellulose (as determined to be a fraction of glucan polymers resistant to mild but not to concentrated sulfuric acid hydrolysis before GC-MS analysis) was also detected but only in small quantities (Fig. 2C). It is expected that amorphous or semicrystalline cellulose would be susceptible to even mild acid hydrolysis to produce glucose. In contrast, crystalline cellulose, while being recalcitrant to mild acid treatment, would be hydrolyzed by exposure to concentrated sulfuric acid. Therefore, our cell wall composition results suggest that the nascent cellulose fibrils, as visualized by fluorescence microscopy (Figs. 1C and 2, A and B), likely contain a substantial fraction of amorphous or semicrystalline cellulose. To gain further validation into the crystallinity of the nascent cellulose on regenerated protoplast cell walls, we labeled CBM17 (a carbohydrate binding module specific to amorphous cellulose) with Alexa Fluor 568, making Alexa568-CBM17. In contrast to the original CBM3a probe developed to bind to both crystalline and semicrystalline cellulose (*27*, *28*, *66*), CBM17 is known to bind exclusively to amorphous or semicrystalline cellulose (*28*, *29*). The protoplasts stained with Alexa568-CBM17 after ~25-hour cell wall regeneration showed fibril network structure that looked very similar to the protoplasts stained with Alexa568-tdCBM3a (fig. S2). We also tested CBM1, known to bind to crystalline cellulose exclusively (*67*–*69*), and found that Alexa568-CBM1 did not show any fluorescence (fig. S2). These results imply that mostly amorphous or low crystallinity cellulose is likely to be predominantly present in the nascently synthesized and assembled CMFs on plant protoplast surfaces after cell wall regeneration under our experimental conditions. While it is likely that the amount of crystalline cellulose present is a minor portion of the total glucan content (2.5 ± 5%; based on the compositional data) and hence could not be detected by CBM1, it is possible that we are overestimating the presence of crystalline cellulose using compositional data alone. Since formation of crystalline regions within cellulose is often an artifact of sample drying (*70*), which is inevitable when performing composition analysis on dried samples using acid hydrolysis, we should be cautious in our interpretation of the crystalline cellulose compositional results. Future work using alternative characterization methods (e.g., Raman spectroscopy) could help further investigate the amorphous versus crystalline nature of nascently synthesized cellulose fibrils formed in protoplasts during cell wall regeneration.

Time-resolved imaging enables real-time tracking of cellulose biosynthesis

Live-cell time-lapse fluorescence microscopy is essential for us to gain full understanding of the dynamic process of how the mature cellulose fibril network (as seen in Fig. 1C) develops over longer time periods (~24 hours) of cell wall biosynthesis at the single-cell level. Despite the extensive microscopy studies conducted on plant cells and tissues over the many decades (*13*–*18*, *32*–*35*, *41*–*53*), continuous visualization of cellulose on the surface of isolated plant protoplast cells during cell wall regeneration has been rarely reported (*54*). This paucity of data can be primarily ascribed to the challenge

in keeping plant protoplasts healthy or viable over a prolonged imaging period, because protoplasts lacking cell walls are often susceptible to mechanical, chemical, and light-induced damages. We used two main strategies for reducing protoplast stress during longer-term live-cell fluorescence microscopy, including (i) in situ cellulose labeling with a low concentration of CBM-based probes like Alexa568-tdCBM3a and (ii) imaging the underside of the protoplast with TIRFM for minimal dose of excitation light and phototoxicity. The TIRFM excitation scheme was also optimal for reducing background fluorescence from unbound dyes in solution and autofluorescence from chloroplasts.

We additionally found that environmental conditions, especially ambient light and temperature, substantially influenced cell wall regeneration, and thus, proper control of these environmental conditions over the entire course of imaging was critical. Protoplasts incubated without ambient light failed to regenerate cell walls, demonstrating the essential requirement for light for cell wall regeneration (fig. S3). To provide protoplasts with controlled ambient light during time-lapse fluorescence microscopy, we synchronized a programmable white LED light bulb (Hue, Phillips) with our microscope such that the bulb automatically switched off and on at the start and end of an image acquisition cycle, respectively. Initially, we found that cell walls were not properly regenerated when protoplasts were incubated on our microscope stage even in the presence of ambient light. We found that the motorized microscope body and stage generated heat (increasing sample temperature to 25°C or higher). We, therefore, developed an active liquid-cooling system for the microscope stage and objective lens to maintain the sample chamber temperature at ~18°C) (Fig. 3A). These modifications eliminated inconsistent cell wall regeneration under longer-term imaging conditions.

TIRFM, combined with CBM-based in situ labeling and active control of ambient light and temperature, enabled us to visualize and image cellulose growth on the underside of the protoplast. To best preserve the native biosynthesis dynamics and the ultrastructure of nascent cellulose deposited on the cell surface, we did not attempt to immobilize protoplasts to the coverslip. Free protoplasts, while sedimented down, typically showed 3D translational and rotational mobility that challenged continuous monitoring of cellulose biosynthesis on a protoplast surface with TIRFM for long time periods (movie S2). Despite low yield of valid long-term imaging data in this condition, we nevertheless could acquire time-lapse images of 14 regenerating protoplasts at 6-min intervals for nearly a day (Fig. 3B and movie S3). The time-lapse images showed that the amount of nascent cellulose increased nonlinearly in time, with an initial "lag" phase—lasting ~10 hours—followed by a "growth" phase (Fig. 3C and fig. S4). Highly mobile, short ($\lesssim$2 μm) cellulose fibril fragments were mainly present in the lag phase, whereas less mobile or stationary networks of longer intertwined cellulose fibrils were predominantly observed during the growth phase. To quantify overall mobility of cellulose fibrils versus time, we plotted normalized cross-correlation (NCC) between two consecutive image frames over time (Fig. 3D, fig. S4, and Materials and Methods). NCC analysis confirmed an interconnection between the mobility and the amount of nascent cellulose fibrils in a biphasic manner (Fig. 3, C and D). High fibril mobility (i.e., low NCC) visible during the early lag phase rapidly decreased (i.e., increased to high NCC) in the later growth phase of cellulose production. Cell-to-cell variability in cellulose biogenesis dynamics can be represented by the error bars in Fig. 3, C and D, with the caveat of small sample size (i.e., 14 cells) taken into account. Overall, similar behaviors were observed among protoplasts whose nascent cellulose on the cell surfaces could be continuously imaged in focus by TIRFM for a long term (movie S4).

Diffusive motions of nascent cellulose fibrils on protoplast surface

The image acquisition at 6-min time intervals used for longer-term TIRFM proved too slow to reveal the details of cellulose fibril dynamics on the surface of the protoplast during distinct stages of cell wall regeneration. When the image acquisition time interval was shortened to once every 20 s, the increased total dose of excitation laser exacerbated phototoxicity of cells and reduced cell viability, preventing longer-term live-cell imaging. As a compromise, we imaged different cell wall regeneration stages for only several hours at 20-s intervals to better understand the dynamics of cellulose network development during different phases of regeneration without overstressing the protoplasts.

Twenty-second interval time-lapse imaging showed random translational and rotational motion of very short cellulose fragments on the protoplast underside during the early stages of cell wall biosynthesis (Fig. 4A and movies S5 and S6). We selected short ($\lesssim$2 μm) fibril fragments, manually tracked their centers in two dimensions, and plotted their mean square displacement (MSD) in time. Fitting the MSD of each trajectory with a power-law scaling in time resulted in a unimodal distribution of the scaling factor "α"—also known as anomalous diffusion exponent—with 0.89 ($\pm$0.05, SE) as the fitted mean value (Fig. 4B). Therefore, the cellulose fragments formed at the early stages of cell wall biosynthesis moved rapidly on the protoplast cell surface according to nearly normal diffusion (i.e., $\alpha \simeq 1$), if not slightly subdiffusive. The closed topology of the spherical cell surface may be at least partially responsible for subdiffusive 2D motion, when the cellulose fibril motion on the 3D spherical surface is projected onto a 2D focal plane in TIRFM imaging.

Coalescence of shorter nascent cellulose fragments to complex fibrils

The short cellulose fibril fragments were not only diffusing on the membrane surface but could also change their shape through rapid interfibrillar interactions. Figure 5A (also see movies S7 and S8) exemplifies such cellulose interfibril coalescence events. It was frequently observed that two short fibrils (labeled "1" and "2" in Fig. 5A) of ~2 μm or less in length encountered each other through surface diffusion. Typically, an end of one fibril first made a contact with the middle part of the other fibril obliquely, and they soon collapsed on top of each other, creating a thicker fibril (labeled "3" in Fig. 5A). The bundle of two coalesced fibrils changed its morphology. For example, the short, thick bundle ("3" in Fig. 5A) later emerged as a longer, thinner fibril possibly through sliding motion between the two merged fibrils (i.e., "1" and "2"). Sliding of cellulose fibrils was observed in previously published AFM studies and proposed to play an important role in building extensible cell walls (*5*, *50*, *71*). Interfibril coalescence also occurred among longer cellulose fibrils (see "3," "4," and "5" labels in Fig. 5A) to generate even longer fibrils. In this case, one fibril could swing around, pivoting on the junction with another fibril until their association was stabilized. On the basis of such observations, we reasoned that the cascade of cellulose fibril coalescences occurring at various fibril length scales could contribute toward building an intertwined cell wall fibrillar framework for less mobile, extended fibril networks. In addition, coalesced cellulose

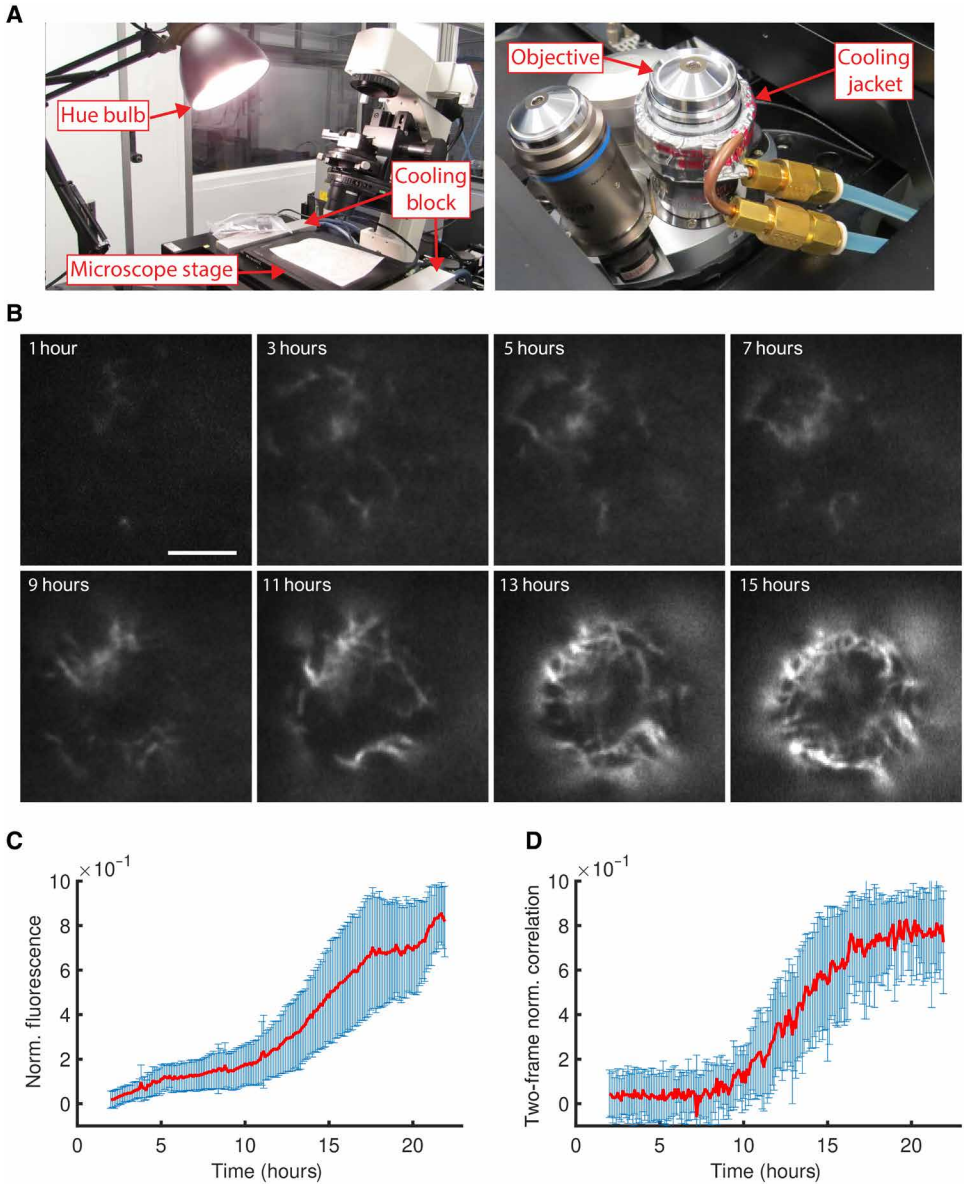

Fig. 3. Live-cell TIRFM to visualize real-time cellulose biosynthesis in protoplasts. (**A**) Pictures of the custom-built imaging instrument parts to control the environmental conditions, i.e., ambient light (left) and sample temperature (right), while acquiring real-time TIRFM images of cellulose that are being synthesized and assembled on protoplast cell surfaces. (**B**) A representative time-lapse TIRFM image sequence visualizing cellulose formation on a protoplast surface. Cellulose was in situ stained with Alexa568-tdCBM3a in the cell wall regeneration media. Image acquisition began 1 hour after the start of cell wall regeneration and continued for ~16 hours at 6-min imaging intervals. Images subsampled at 2-hour intervals are shown here (see movie S3 for the full image sequences for this cell and additional 13 cells). (**C** and **D**) Normalized total fluorescence (C) and normalized cross-correlation (NCC) (D) in time obtained from the time-lapse image data of 14 cells shown in movie S3. Red curves and blue error bars here indicate the average and the SD of the 14 individual cell data shown in fig. S4. Total fluorescence and NCC (see Materials and Methods for definition) quantitatively estimate the total amount and the overall mobility, respectively, of cellulose on the protoplast surface that can be observed by TIRFM. A lower NCC value implies a higher fibril mobility and vice versa. Scale bar, 5 μm.

fibrils can show highly dynamic reshaping of their morphology (Fig. 5B and movie S9). Cellulose fibrils can also exhibit remarkable dynamics of bending and unbending (Fig. 5C and movie S10) such that a fibril could self-coalesced through ~180° bending (movie S11). It was apparent that the dynamic morphological plasticity and the "sticky" noncovalent interactions between cellulose fibrils could play important roles in driving the self-assembly of a sparsely interconnected primordial cellulose fibril network observed herein, which we termed "proto-network," as a potential precursor to the final mature, dense cellulose fibril network (movie S8).

Progressive elongation of fibrils drives network cross-linking and densification

Cellulose fibrils are thought to be synthesized by mobile CSCs on cell membrane surfaces (*8*, *9*), and as such, we expect to observe actively growing fibrils on the protoplast surface. However, we rarely

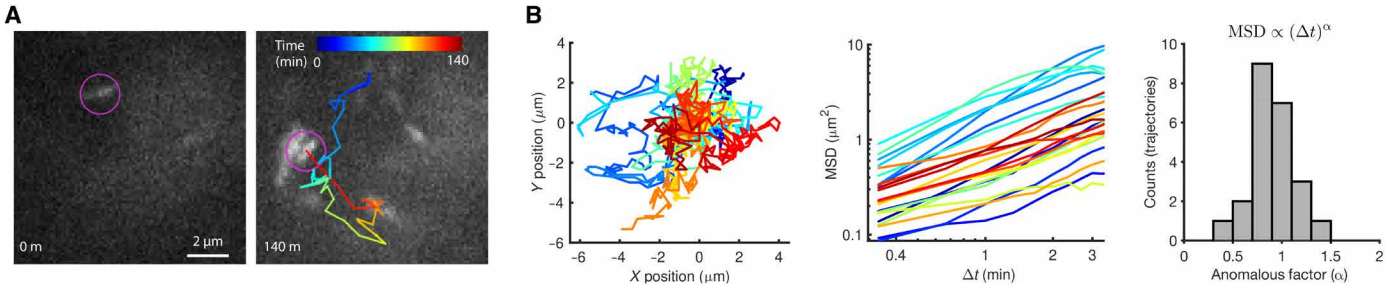

Fig. 4. Diffusive motion of short cellulose fragments can be seen in the early cellulose biosynthesis and cell wall regeneration stage. (**A**) Trajectory of the center of a representative short cellulose fragment moving rapidly on the surface of an *Arabidopsis* protoplast at the early stage of cell wall regeneration. The colormap represents the tracking time (see movie S5 for the full image stack and movie S6 for additional data). Cellulose was imaged on the surface of regenerating *Arabidopsis* protoplasts through in situ staining with Alexa568-tdCBM3a and TIRFM. (**B**) Left: 2D trajectories of randomly moving 23 short fibrils (≲2 μm in length) observed in nine protoplasts. The trajectories were colored arbitrarily and centered at the origin of *XY* axes for better visualization. Middle: Log-log plot of MSD in lag time for the 23 trajectories. The temporal scaling factor of MSD (i.e., anomalous diffusion exponent) was obtained by linear fitting of this plot. Right: Histogram of anomalous diffusion exponent for the 23 trajectories (mean = 0.89, SD = 0.24). Scale bar, 2 μm.

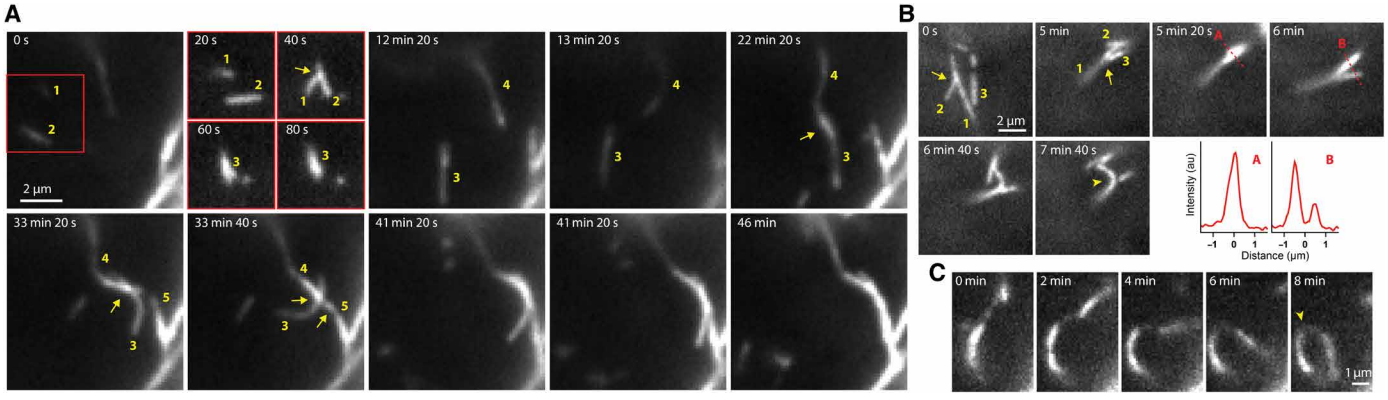

Fig. 5. Coalescence of nascently synthesized cellulose fibrils can lead to generation of thicker and/or longer fibrils on the protoplast surface. (**A**) Time-lapse images showing a cascade of interfibril coalescence events that led to assembly of a stable, extended, and thicker cellulose fibril. These images are subsampled from movie S7 that was acquired at 20-s intervals. The second panel shows four image sequences of the subarea in the first panel indicated by a red square. Relevant fibrils are numbered in yellow to identify coalescence events, e.g., 1 and 2 fibrils coalesce into 3. Similar cellulose coalescence events commonly occur and facilitate self-assembly of fibril networks as observed in many cells (see movie S8). (**B**) An example of coalesced cellulose fibrils showing dynamic morphological changes (see movie S9 for the full image stack). (**C**) Images of an extended cellulose fibril showing dynamic bending and unbending (see movie S10 for the full image stack). The yellow arrow (B) indicates the junction of fibril coalescence. The yellow arrowhead (B) and (C) indicates the point of high curvature. Cellulose was imaged on the surface of regenerating *Arabidopsis* protoplasts by in situ staining with Alexa568-tdCBM3a and TIRFM. au, arbitrary units.

observed such events in the early stages of cell wall biosynthesis (<10 hours) when highly mobile short fibril fragments were prevalent. As described previously, small fibrils were rapidly diffusing, tumbling, and frequently disappearing out of focus, which made it technically difficult to track short fibril length changes. It was not until the emergence of a proto-network (~10 hours after the start of cell wall regeneration) that distinct processive synthesis, elongation, and deposition of single fibrils were clearly observed. Figure 6A and movie S12 show such events of single fibril biosynthesis observed in protoplasts. Such newly synthesized fibrils were often seen to be anchored to the relatively immobile proto-network on one end, while their length grew processively on the other end. Diffusive motion was still apparent in the actively growing fibrils, but the active adherence of the growing fibrils to a stable underlying proto-network substantially reduced the random motion as compared to freely diffusing short cellulose fragments seen otherwise (Fig. 6B). A single growing fibril sometimes encountered another growing fibril, and they both fused to form a bridge between two anchor points on the existing fibril network (Fig. 6C). Fibrils also grew and crossed over other stationary, formerly deposited fibrils, creating a point-like coalescence at each junction (Fig. 6D). Therefore, active growth and processive deposition of single fibrils played important roles in interconnecting and cross-linking the underlying proto-network to develop an increasingly dense and stable cellulose fibril network on the protoplast surface. On the basis of our time-lapse microscopy data, the processive growth rate of a single fibril was estimated to be ~0.13 (±0.04, SD) μm/min (fig. S5). This rate, although slightly slower, is in the similar range as the previously reported speed of CESA/CSC (~0.20 to 0.40 μm/min) movement measured in plant tissues that was supposedly coupled to cellulose synthesis (*46*–*48*).

Cellulose proto-network evolution to more compact and stable states

We observed that the ultrastructure of the newly assembled proto-network continued to change even after its emergence (Fig. 7 and movie S13). Certain local areas of the proto-network, especially

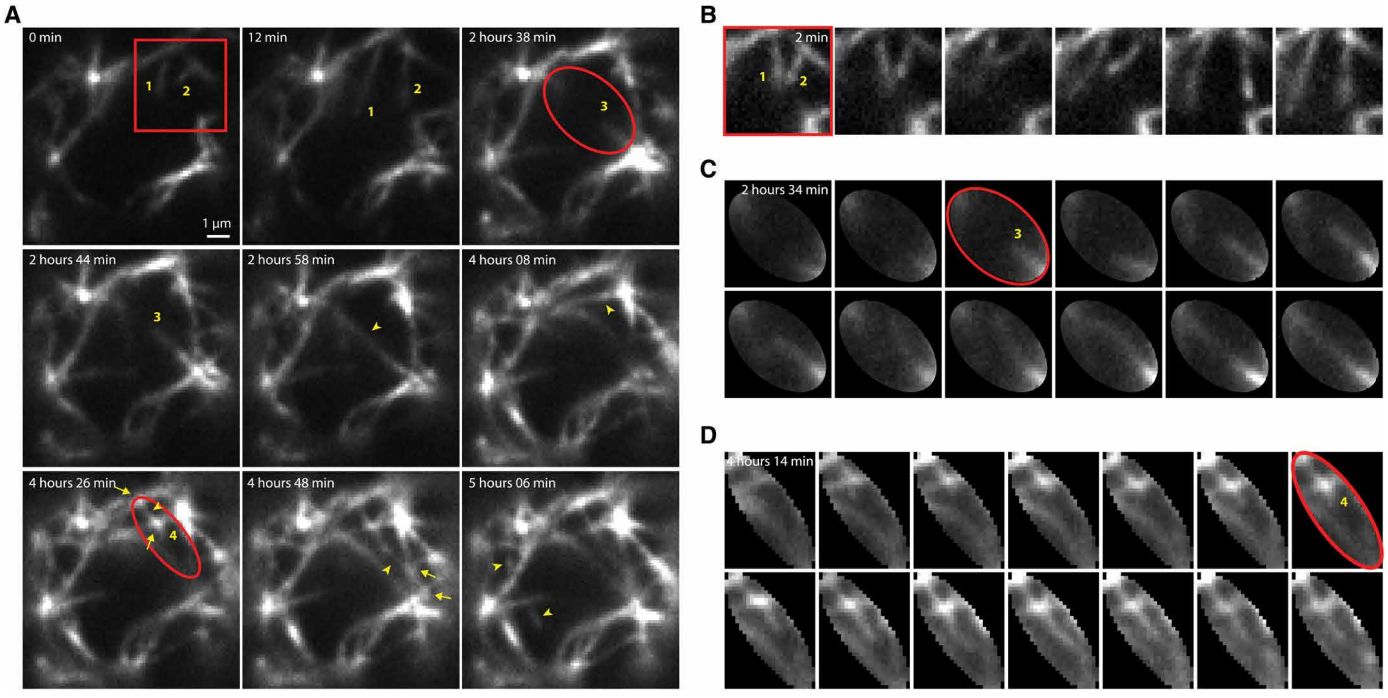

Fig. 6. Observation of real-time processive biosynthesis of single cellulose fibrils on the protoplast surfaces using TIRFM. (**A**) Time-lapse images showing processive growth of single cellulose fibrils on the protoplast surface (see movie S12 for the full image sequences for the cell shown in this figure and three additional cells). The image acquisition started after 16-hour cell wall regeneration. The representative growing fibrils are marked by yellow numbers. Yellow arrowheads indicate the fibril segments that newly appeared upon processive fibril synthesis and extension. Yellow arrows indicate the coalescence junctions newly formed by actively growing fibrils that cross over underlying preexisting fibrils. (**B** to **D**) Detailed image sequences of three subareas in (A) that are highlighted by a red box and two ovals. The time interval between two consecutive images is 2 min in (B) to (D).

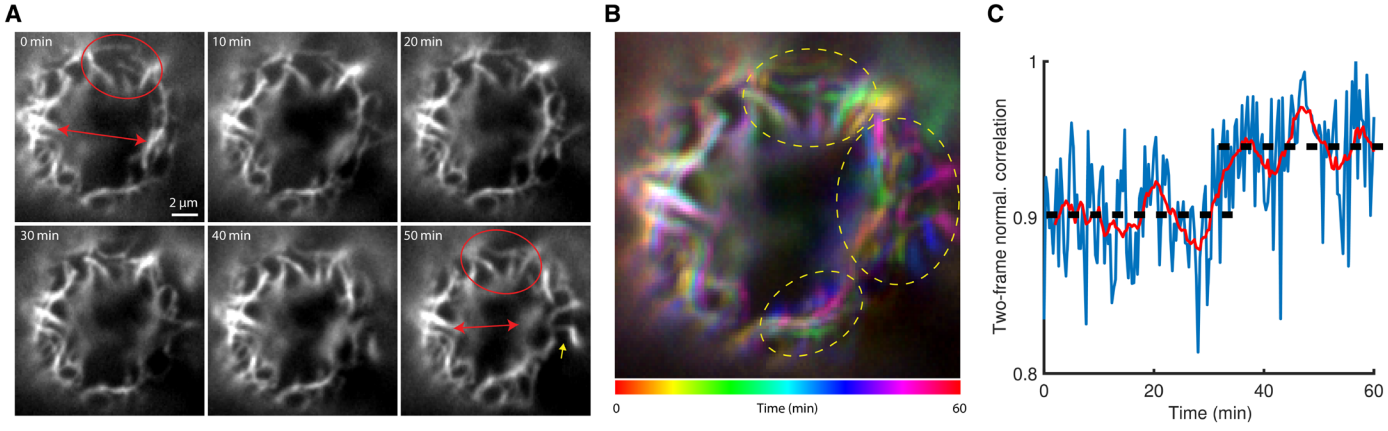

Fig. 7. Cellulose fibril network continues to mature and reshape on the cell surface. (**A**) Time-lapse images of a cellulose fibril network with a morphology that slowly but continuously changes as the cell wall regeneration process goes to completion (see movie S13 for the full image sequences for the cell shown in this figure and 10 additional cells). The initial coarse mesh of fibrils within a highlighted area (red oval) turned into a more refined mesh within 50 min. The initial distance between two specific locations on the fibril network (red arrow) got shorter by intrusion of another fibril segment indicated by yellow arrow (see movie S13 for the detail). (**B**) 2D projection of the time-lapse images with temporal color coding to visualize the local mobility of fibril network. Mobile regions appear in rainbow color (dotted ovals), whereas stationary regions in white color. (**C**) NCC shows a trend of slow but increasing values in time, implying evolution of the network toward a more stable ultrastructural configuration. Blue curve represents the original 20-s interval time-lapse data. Red curve represents the moving average of the blue curve with a sliding window of 4-min width. Scale bar, 2 μm.

where the overall matrix mesh was relatively coarse, appeared more mobile and unstable than other areas (Fig. 7B). Fibrils in these areas showed pronounced diffusive motion and bending dynamics; furthermore, they could deform into a more compact appearance by mechanical pressure from the neighboring parts of the fibril network that could be more rigid (Fig. 7A). NCC analysis plots of the time-lapse images implied that such densification and refinement of the fibril mesh ultimately results in a more stationary, stable cellulose networks (Fig. 7C). Therefore, the cellulose fibrillar network appears to be evolving slowly (i.e., more than 10 hours) but continuously to form a more compact and stable multilayered structure on the protoplast membrane surface.

Intricate cellulose fibrillar network revealed by super-resolution microscopy

The distinctive CSC structure, a six-lobed rosette CESA trimer, implies that 18 cellulose chains are likely to assemble and bundle into a cellulose elementary fibril (*8*, *9*). AFM and other imaging methods have measured ~3 to 5 nm in diameters of elementary fibrils, which is consistent with cellulose microcrystal fibril packing models of 18, 24, or 36 cellulose chains (*4*, *10*). Moreover, elementary fibrils are thought to merge into bundles with various diameters of less than 100 nm, termed "microfibrils" (*4*, *10*, *11*). Because of the diffraction-limited optical resolution, it was unclear whether our TIRFM images of cellulose fibrils on the protoplast surface represented elementary fibrils, or microfibrils, or even bundles of microfibrils. To visualize the cellulose fibril network in higher resolution, we applied stochastic optical reconstruction microscopy (STORM) (*40*), a super-resolution fluorescence microscopy technique in the category of single-molecule localization microscopy (SMLM) (*39*, *40*). We found that Alexa568-tdCBM3a "blinked" very well under STORM imaging conditions, which is the most critical requirement for identifying and localizing single molecules in SMLM (movie S14 and Materials and Methods). While we were trying to immobilize live protoplast cells—large spherical objects of 40 to 50 μm in diameter—on a poly-L-lysine–coated coverslip for STORM imaging, the entire cellulose fibril network was found to be susceptible to detachment from the cell surface through hydrodynamic drag forces. We serendipitously discovered that during detachment, protoplasts peeled in a way as to leave behind a wide area of the cellulose fibril network on the poly-L-lysine–coated coverslip surface. We further developed a procedure to optimally imprint a large area of cellular surface cellulose network on the coverslip while largely preserving native structure (fig. S6A). The cellulose-visible area of ~35 μm in diameter implied that the cellulose fibrils network covering approximately a quarter of the original protoplast surface was readily transferred to the coverslip. This was a much larger area than the ~10-μm-diameter area of the protoplast bottom surface that could be typically imaged by TIRFM in focus. The imprinted cellulose fibril network looked similar to those of intact cells, and we postulated that 2D-STORM images of the imprinted cellulose could provide insights into the high-resolution architecture of regenerating protoplast cellulose fibril network while avoiding the challenges in 3D-STORM imaging of thick objects such as intact plant protoplast cells (*72*, *73*).

We acquired STORM images for both *prc1-1* (*cesa6* knockout mutant) and wild-type *Arabidopsis* plant lines with Alexa568-tdCBM3a probe. tdCBM3a (~46 kDa) has a hydrodynamic radius of 3.1 nm based on its molecular weight (*74*), which is ~3 to 4 times smaller than typical antibodies used for immunolabeling. The small size of Alexa568-tdCBM3a probe is likely to contribute to optimal STORM resolution. Our high-resolution STORM images revealed an intricate reticulated network of cellulose fibrils on the protoplast surface after 48-hour cell wall regeneration in both the plant lines (Fig. 8 and fig. S7). Single fibrils in STORM images appeared as much thinner lines ($\lesssim$50 nm) than in TIRFM images (Fig. 8A). A seemingly single fibril in TIRFM images was frequently found to actually consist of multiple fibrils in STORM images (Fig. 8B and figs. S6B and S7). A layer of cellulose fibrils in plant cell walls is often seen to orient in a certain direction, as in the case of onion epidermis, *Arabidopsis* petioles/hypocotyl/roots cells, and other plant systems (*4*, *15*, *18*, *22*, *23*). In contrast, the fibrils seen in our STORM images did not show any seemingly preferred orientation in regenerating protoplasts but instead formed a highly reticulated network like knitted cloths, fish nets, or trellis. Fibril density or mesh size in the network was heterogeneous, with the fibrils in coarse mesh areas appearing as more curved than in fine mesh areas (fig. S6B). We further identified various types of interfibril associations in the assembly of the fibril network (Fig. 8, C and D, and figs. S6B and S7). A junction between two crossing fibrils was the prevalent type [arrow symbol in Fig. 8 (C and D) and fig. S6B], which was likely to be formed by an actively growing fibril deposited across an underlying stationary fibril as seen in the case of Fig. 6D. It was also common for the convex side of a curved fibril to tangentially coalesce with another straight or curved fibril [two-headed arrow symbol in Fig. 8 (C and D) and fig. S6B]. In this case, the fused segment appeared as a single, brighter line within the STORM resolution limit. Such an organization might have resulted from a lateral encounter and fusion between two dynamically bending/unbending long fibrils that were either freely diffusing (Fig. 5) or tethered to the underlying network (Fig. 7). STORM images could differentiate two very close but noncoalesced fibrils [chevron symbol in Fig. 8 (C and D) and fig. S6B] from the truly fused or coalesced ones. The motion of such closely juxtaposed but noncoalesced fibrils might have appeared as reversible coalescence events seen in the lower resolution TIRFM images or movies (Fig. 5B). In some cases, two fibrils remained closely apart (<200 nm) over ~1.5-μm segment between the fused ends on both sides, resembling a highly stretched loop (Fig. 8E). We also observed similar cellulose fibril bifurcation patterns under scanning EM (Fig. 8F). Typically, two fibrils branched out of a bundled segment, but branching of even more fibrils was also observed (see the dotted circle in fig. S6B).

As the curvature of cellulose sheet changes from spherical to planar during imprinting, extra mechanical tension would build up. The tension could either persist in the form of promoting cellulose fibril bending or be relieved by reorganization of network driven by fibril motions such as sliding, straightening, and bundling/unbundling (*5*, *50*, *71*). Whether the organization structure of an imprinted cellulose network observed with STORM is altered from its native structure on the spherical protoplast surface requires further experimental verification.

DISCUSSION

Textbook plant cell model schematics typically represent plant primary cell walls as cellulose fibrils tethered by hemicellulose inside an amorphous pectin hydrogel matrix (*75*). This simple cartoon model, which is based on limited evidence collected over the past hundred years, has been challenged and revised by several experimental/

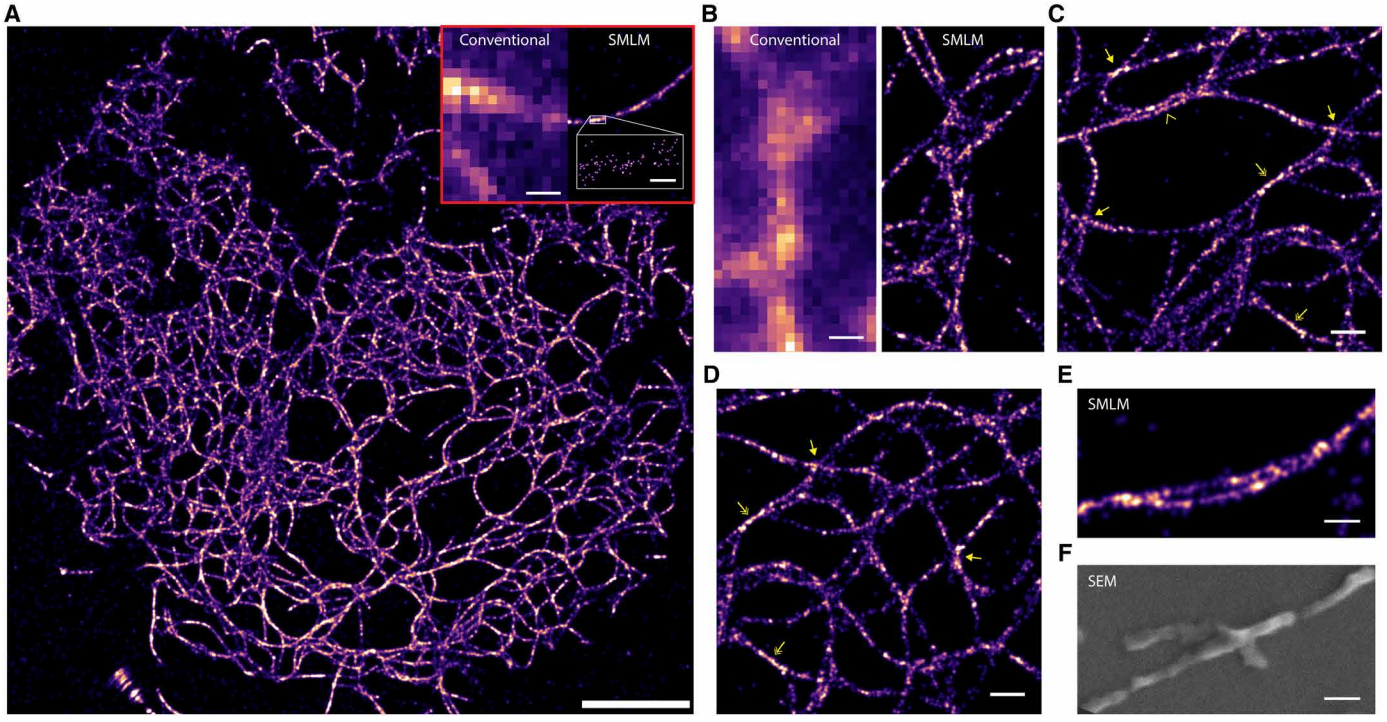

Fig. 8. Super-resolution 2D images of the protoplast cellulose fibril network imprinted on glass coverslips. (**A**) STORM, also known as SMLM, image of cellulose fibril network that was peeled off a protoplast cell—after cell wall regeneration for 48 hours—and adsorbed onto the poly-L-lysine–coated coverslip surface. Cellulose was labeled with Alexa568-tdCBM3a. Alexa568 was induced to blink (see movie S14) under strong 561-nm excitation and STORM buffer (Materials and Methods), and single molecules were identified and localized to reconstruct the STORM image. Inset: Comparison of TIRFM (left) and STORM (right) images of a single CMF. (**B**) TIRFM (left) and STORM (right) images of closely located multiple fibrils. The cellulose network was heterogeneous in the mesh size, with areas of coarse (**C**) and fine (**D**) cellulose fibril mesh sizes that were seen to coexist. Various types of interfibril associations could be identified from the STORM images: cross-coalescence (arrow), tangential fusion of two curved fibrils (two-headed arrow), and close but noncoalesced two fibrils (chevron). (**E**) A bundle of two fibrils maintaining a double-stranded fibril segment (~1.5 μm) in the middle. (**F**) Scanning electron micrograph (SEM) of a branching cellulose fibril extracted from regenerated protoplast cell walls. Scale bars, 5 μm (A), 0.5 μm (inset, left), 50 nm (inset, right), 0.5 μm [(B) to (D)], and 0.25 μm [(E) and (F)]. The protoplast shown here is derived from prc1-1 (cesa6 knockout mutant) transgenic *Arabidopsis* plant line. Similar STORM images for a protoplast derived from wild-type plant line are shown in fig. S7.

modeling studies, advancing our understanding of how cell walls can give rise to the remarkable mechanical properties critical to support plant growth, development, morphogenesis, and function (*5*). However, cell wall studies to date have focused mainly on molecular architecture of the existing or already matured cell wall types in various plant tissues and developmental contexts; hence, little is known about the dynamic processes through which the primary cell wall is constructed in vivo from the cellulose building blocks and developed into the complex ultrastructures as observed by microscopy. In this work, we directly visualized how the *Arabidopsis* protoplast develops a new cellulose fibril network on the cell surface during cell wall regeneration. We could spatiotemporally resolve the dynamics of this process by directly imaging nascent cellulose biosynthesis, fibrillar growth, and assembly into a fibrillar network over extended time periods (i.e., continuously for ~1 day at 6-min imaging intervals or for several hours at 20-s imaging intervals) via tdCBM labeling and TIRFM. On the basis of our findings, we propose a four-stage model for cellulose fibril network development during cell wall regeneration on plant protoplast surfaces (Fig. 9).

First, nascent cellulose fibrils are synthesized as relatively short fragments ($\lesssim$2 μm) and deposited on the cell membrane surface upon initiation of cell wall regeneration (stage ① in Fig. 9). These fragments look to first emerge as a very faint small fluorescent dot of diffraction-limited size and then gets brighter and elongated while moving on the cell surface (fig. S8). Because cellulose can be fluorescently labeled only outside the cell in our TIRFM imaging, it is not clear whether these emergent fragments are formed inside the cell and then exported out, or they are synthesized across the cell membrane by CSCs. The roughly estimated elongation rate from fig. S8 looks comparable to the growth rate of longer cellulose fibrils shown in Fig. 6. Therefore, it is likely that the short fragments are synthesized across cell membrane by CSCs through catalytic glycosyl monomer addition steps. These cellulose fragments randomly diffuse on the surface of the plasma membrane (Fig. 4). At this time, it is not clear whether the observed short fragments are free cellulose fibrils, or they are tethered to the plasma membrane–bound CESA/CSC and undergo active, albeit slow, synthesis/growth while diffusing randomly on the surface. In previous studies, CSCs labeled with fluorescent protein tags were also found to move either along or independently of cortical microtubules in plant tissues (*46*, *48*). The pattern of random translational/rotational motion of the small cellulose fragments in our data seems to be incompatible with the microtubule-guided CSC motion model; it rather implies that either free cellulose is released from CSC to be randomly deposited on the

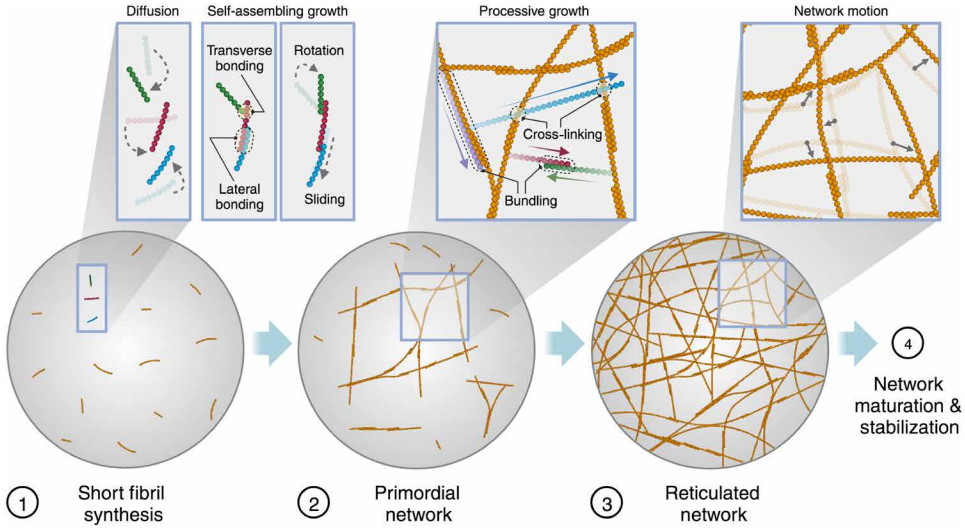

Fig. 9. Proposed model for cellulose biosynthesis and fibril network development during cell wall regeneration in plant protoplasts. Plant protoplasts regenerate the cellulose network during multiple stages of development in this proposed model. Cellulose elementary fibrils synthesized by CSC in short lengths dynamically diffuse and coalesce together to form thicker and long fibrils in stage 1. A less mobile primordial or proto-network emerges from this self-assembly process in stage 2, which is accompanied by more frequent processive cross-network synthesis events of new single cellulose fibrils, generating a highly reticulated network with denser and finer mesh sizes in stage 3. The fibrillar network slowly and continuously rearranges during cell wall regeneration, which helps its shape to mature and evolve into a more compact/rigid/stable network in stage 4.

cell membrane surface and/or that a short cellulose fibril can remain tethered to CESA/CSC while moving independently of microtubules. Both models could explain observed diffusive motion of short fibrils (Fig. 4), although the origin of this phenomenon needs to be further examined in the context of its correlation with CSC and/or microtubule motions by multicolor fluorescence imaging studies in future work.

Second, the highly mobile cellulose fragments, which are produced in the first stage, frequently encounter each other as they diffuse on the cell surface and then coalesce together to form thicker and/or longer fibrils (Fig. 5A) that can further self-assemble into a primordial fibril network (i.e., proto-network) with slower mobility and coarse mesh (stage ② in Fig. 9). Our data suggest that fibril-fibril assembly is predominantly driven by direct cellulose-cellulose interactions between fibrils undergoing rapid diffusion on the cell surface (see further discussion below). Hydrogen bonds, dispersion force, and hydrophobic interactions may be responsible for such cellulose interfibril interactions that drive the formation of a self-assembled cellulose fibril proto-network (*76*–*78*).

Third, processive synthesis of new cellulose fibrils across previously deposited fibrils in the proto-network makes the mesh denser, generating a reticulated network (Fig. 6 and stage ③ in Fig. 9). Processive cellulose fibril elongation is rarely observed for fast diffusing small cellulose fragments at early time periods of regeneration ($\lesssim$10 hours), although it is partly because their frequent disappearance from a narrow TIRFM field of view in both *xy* and *z* direction makes it technically hard to track their length changes, if any. Processive fibril growth occurs more frequently upon emergence of a proto-network, wherein growing cellulose fibrils are mostly tethered to the underlying stationary cellulose network. This biphasic behavior in cellulose synthesis rate is reflected in the temporal change of total Alexa568-tdCBM3a fluorescence seen per single cell in TIRFM data, showing a lag phase of about 10 hours before a fibril network pattern emerges (Fig. 3, B and C).

Moreover, new fibrils typically grow across the underlying fibrils after the lag phase. Such crossover motions are indicative of CSC trajectories generated by the cortical microtubule guidance mechanism (*48*), although it needs to be further verified by colocalization study of cellulose fibrils and microtubules via two-color fluorescence imaging of live cells in future work. The two types of CSC guidance—autonomous and microtubule guidance systems (*48*)—may be at play in the biphasic cellulose synthesis behavior observed during cell wall regeneration. It is possible that a CSC, while actively synthesizing cellulose, either through autonomous or microtubule guidance mechanism, may be susceptible to destabilization, inactivation, and/or disassembly when the nascent cellulose fibril emerges untethered, resulting in highly fragmented cellulose fibril products early in cell wall regeneration. In contrast, CSC may be able to more stably and steadily synthesize longer cellulose fibrils, being guided along a microtubule, when the nascently growing fibril is attached to a semi-stationary proto-network that is constructed by the self-assembly mechanism (stage ② in Fig. 9). Hence, formation of a primordial cellulose fibril network (i.e., proto-network) after the initial lag phase likely provides a crucial template for additional microtubule-guided robust, processive cellulose synthesis by CSC to more effectively develop the final interwoven fibril networks.

Last, the self-assembled proto-network superstructure is not stationary but rather it is dynamic, capable of slowly and continuously rearranging its shape to become a more compact/rigid/stable network (Fig. 7 and stage ④ in Fig. 9). Previously published work has identified three distinctive types of CMF motions (both experimentally in cell wall stretching assays and computationally in coarse-grained molecular simulations)—sliding, straightening, and changes in bundling. These distinct types of motions were proposed to explain the mechanical response of the cell wall to external forces

(*50*, *71*). They are also likely to be involved in the cellulose network dynamics observed in our study, possibly playing important roles in relieving any local buildup of mechanical stress that may occur while nascent cellulose is continually deposited on the protoplast surface during cell wall development.

It needs to be emphasized that the model proposed in Fig. 9 can be directly supported by our experimental data only at a phenomenological level, largely in terms of apparent cellulose biogenesis dynamics observed by time-lapse TIRFM, while leaving open questions about the underlying mechanistic details. Particularly with regard to the cause and structure of the actively growing CBM3a-reactive polysaccharide in our microscopy data, it was rationalized as representing a cellulose elementary fibril synthesized by CSC, based on now accepted scientific dogma. Such a speculation should be experimentally verified by studying the spatial relationship between CSC and cellulose with two-color TIRFM microscopy and investigating the nanoscale structure of cellulose fibrils on the protoplast surface with ultrahigh resolution nanoimaging methods such as AFM or TEM in future work. Nevertheless, the proposed model primarily focuses on a unique dynamic process of cellulose network development on the protoplast surface in which diffusion and self-assembly play critical roles. This aspect of the model will be largely independent of the underlying mechanistic details at the molecular and nanoscale level.

A model of the primary cell wall as a collection of well-separated CMFs mechanically tethered by xyloglucan polymer bridges (*64*) is widely accepted. However, whether xyloglucan plays a major load-bearing role has been called into question by studies of xyloglucan-deficient *Arabidopsis* double mutants (*xxt1/xxt2*), which showed only minor effects either on growth and appearance of the mutant plant (*62*) or on cell wall regeneration of the mutant protoplast (*53*). An alternative model postulates that CMFs make tight contacts between each other to form cellulose-cellulose junctions, termed "biomechanical hotspots," that play key structural and mechanical roles in formation and stabilization of the primary cell wall (*5*, *79*). Such junctions could originate from either direct inter-cellulose interactions or mediation, at least in part, by xyloglucan. Our time-lapse TIRFM data (Figs. 3, 5, and 6) and STORM images (Fig. 8) confirm the existence of junctions between cellulose fibrils; moreover, they uncovered the dynamic processes by which such junctions form through fibril coalescence, yielding stable cellulose fibril networks on the cell surface. To investigate the role of xyloglucan in cellulose fibril coalescence and cell wall development, we acquired time-lapse TIRFM images of cellulose in xyloglucan-deficient *Arabidopsis* double mutants (*xxt1/xxt2*)-derived protoplasts during cell wall regeneration (fig. S9 and movie S15). Mutant protoplasts showed cell wall regeneration behaviors very similar to wild type, suggesting the primary role of direct cellulose-cellulose interaction in the formation of interfibril junctions despite the absence of xyloglucan. However, since we see a notable increase in mannose and xylose containing polysaccharides after cell wall regeneration, it is still possible that minor hemicellulosic components like glucomannans could interact with cellulose to provide functional redundancy for xyloglucan as suggested by a recent study (*80*).

Protoplasts have been used as a powerful tool for nearly six decades to study various molecular and cellular processes such as cell wall synthesis, regeneration, and modulation against intrinsic and extrinsic stress factors (*81*, *82*). However, removal of the cell wall is known to activate stress/wounding response and genes for metabolic process functions (*83*, *84*), which can be a major limitation of using isolated mesophyll protoplasts as a proxy to understand the mechanism of cell wall biosynthesis as compared to intact or natural plant tissues undergoing cell wall growth. It is possible that the mechanism of cell wall biosynthesis during normal plant cell development could be distinct from that observed using isolated protoplast cells. In addition, the protoplasts were plasmolyzed in hypertonic cell wall regeneration media containing 0.5 M Mannitol during our time-lapse TIRFM imaging to prevent cell lysis from osmotic pressure. In contrast, the plasma membrane of a normal turgid plant cell is pressed against the cell wall. The lack of both existing cell walls and turgor pressure in the protoplasts may affect the cellulose fibril network assembly process in ways that promote altered behaviors, such as abrupt movements of short fibrils and cross junction fibril elongation either directly from the pressure change itself or indirectly from the potential alteration in cortical microtubule dynamics and/or CSC dynamics as compared to turgid cells.

Nevertheless, protoplasts competent for cell wall regeneration provide a unique opportunity at this time to enable the study of in vivo cell wall biogenesis, with minimal background from a preexisting cell wall matrix. The protoplast system makes possible the stepwise description of the dynamic processes that could facilitate evolution and self-assembly of the intricate cell wall, starting with short, highly diffusive cellulose fragments. In native plant cells, the primary cell wall is made de novo in daughter cells during cytokinesis via cellulose deposition on the cell plate—the primordial daughter cell membrane rich in callose and transient microtubules. Although turgor pressure is likely to play a less important role in this case, the callose scaffold and microtubule dynamics unique to the cell plate may affect the cellulose assembly dynamics. Whether the processes that we described here for regenerating protoplast also take place during some context of normal development, such as cell division and cytokinesis, will have to await new techniques (e.g., deep tissue imaging) that could overcome the background issues posed by preexisting cell wall materials.

In summary, we developed a live-cell imaging system to observe cellulose formation and fibrillar assembly on the surface of plant protoplasts undergoing cell wall regeneration. Combining fluorophore-labeled tandem CBM3a, TIRFM imaging, and ambient light/temperature control enabled us to continuously monitor the dynamics of nascent CMF synthesis and development toward a network during the initial ~1 day of cell wall regeneration in high spatial and temporal resolution. The findings captured by our study provide important insights into dynamic aspects of plant cell wall and cellulose fibril synthesis at the single-cell level. Our microscopy platform and experimental workflow will also be suitable for studying the correlative dynamics of other cell wall components going beyond the role played by cellulose in live plant protoplasts.

MATERIALS AND METHODS

Plant materials and growth conditions

Arabidopsis thaliana Col-0 (Columbia) was used for all wild-type or transgenic control experiments. Seeds of Col-0 were purchased from ABRC (Arabidopsis Biological Resource Center). Approximately 50 seeds were incubated in 10% bleach for 5 min, washed thrice with excess sterile distilled (DI) water, and resuspended in 50 μl of DI water before germination. Sterilized seeds were poured onto Murashige and Skoog media plates supplemented with Gamborg's

vitamins (Phytotech Lab, M404). Seeds were spread evenly using a sterile pipette tip and incubated at 4°C and ambient humidity for maximum 3 days. Plates were later transferred to the plant growth chamber at 23°C, with a light intensity of 120 to 150 μmol/m^2 per s with 40 to 65% relative humidity and a 10-hour photoperiod consisting of 10 hours of light and 14 hours of dark photoperiod. Seedlings were allowed to grow for 8 to 10 days before transferring into pots with promix soil (Grinffin, BK25-V) and incubated in the growth chamber with the same conditions. All other reagents were purchased from VWR International, Thermo Fisher Scientific, and Sigma-Aldrich unless mentioned otherwise.

Arabidopsis mesophyll protoplast isolation

Mesophyll protoplasts were isolated, as described by Yoo *et al.* (*82*), with slight modifications as described here. Briefly, 3- to 4-week-old fully expanded leaves of *Arabidopsis* plants (as shown in Fig. 2A) were selected. The selected leaves were uniformly sized to avoid heterogeneity in the size of protoplasts. Leaf strips (0.5 to 1 mm thick) were cut off from the middle part of a leaf using sharp and sterile razor blades (single-edged blade; VWR International, catalog no. 55411-055) without any damage to the tissue at the cutting site. The leaf strips were quickly transferred into a sterilized enzymatic solution [0.4 M Mannitol, 20 mM KCl, 20 mM MES, 1.5% Cellulase R10 (Yakult Pharmaceutical Ind. Co. Ltd., Japan), 0.4% Macerozyme R10 (Yakult Pharmaceutical Ind. Co. Ltd., Japan), 10 mM $CaCl_2$, 5 mM 2-mercaptoethanol, and 0.1% bovine serum albumin (BSA)] using flat-tip forceps and submerged completely. The leaf strips were vacuum-infiltrated for 30 min before incubating the samples in the dark for a maximum of 5 hours for enzymatic digestion. Upon incubation, the protoplasts were diluted with an equal volume of sterile W5 solution (154 mM NaCl, 125 mM $CaCl_2$, 5 mM KCl, and 2 mM MES in double-distilled water). The undigested leaf tissues were removed by filtering the solution through a prewashed nylon mesh (75 μm, laboratory sifters, Carolina Biological Supplies, catalog no. 65-2222N). Protoplasts were collected by spinning at 207 relative centrifugal force (rcf) for 3 min at 4°C. The isolated protoplasts were washed twice with 10 ml of W5 solution to remove any residual enzyme solution. Last, the protoplasts were resuspended in 0.5 ml of W5 solution. The quality of the protoplasts isolated was routinely observed under the regular light microscope (Fig. 1). The quality of protoplasts was deemed unsuitable if they were too large (>100 μm), too small, or broken/lysed. As a rule of thumb, medium-sized leaves were chosen for isolation to generate protoplasts with overall size in the range of 30 to 50 μm under bright-field microscopy. The concentration of protoplasts was measured using a hemocytometer (Hausser Scientific, catalog no. 1483), and the final concentration was adjusted to 2×10^5 protoplasts ml^{-1} of W5 solution. The freshly isolated protoplasts were stored on ice for immediate use for experiments typically within 2 hours or in a 4°C fridge for experiments in the following day.

Protoplast cell wall regeneration on lab bench

Approximately 200 μl of protoplasts of concentration 2×10^5 protoplasts ml^{-1} were used for the cell wall regeneration experiments. The protoplasts were gently pelleted down at 207 rcf for 2 min using a refrigerated centrifuge (4°C). The supernatant was removed, and the protoplasts were then stored in a WI solution media solution (4 mM MES, 0.5 M mannitol, and 20 mM KCl). Cell wall regeneration media (WI/M2) contains an equal volume of WI and M2 media [Gamborg's B-5 basal medium with minimal organics (6.4 g/liter) from Sigma-Aldrich, 0.8 M trehalose, 0.1 M glucose, and 1 μM 1-naphthalene acetic acid (pH 5.7)] (*51*). The protoplast suspension in cell wall regeneration media was incubated at room temperature (20° to 23°C) under continuous ambient light exposure conditions (Philips hue lamp) over 24 hours.

Protoplast sample preparation for cell wall glycan composition analysis

Approximately 1.5 mg of air-dried (18 hours in oven at 56°C) protoplasts was transferred into a 2-ml reaction tube (Sarstedt). To remove the cell wall regeneration media components, the samples were washed with 1 ml of double-distilled water and vortexed for 15 s at maximum speed (>13,000*g*) in a mini-centrifuge. The aqueous phase is collected at each step for analysis. The protoplasts were then recovered after washing by centrifuging into a pellet at 10,600*g* for 30 s. The supernatant was removed carefully without disturbing the solid pellet. Samples were then washed with 1 ml each of 70% (v/v) ethanol followed by chloroform:methanol (1:1, v/v) mixture in series. Following that, the sample was resuspended and washed twice with 1 ml of double-distilled water. All aqueous phase fractions were pooled together and filtered using 0.2-μm nylon syringe filters. One milliliter of the aqueous extract was evaporated in vacufuge and lyophilized overnight. Alternatively, the washed protoplasts were also placed inside a lyophilizer (Labconco FreeZone 4.5) for drying overnight. Last, the samples were washed with 1 ml of acetone to collect the residual pellet samples stuck to the walls of the tube and dried overnight. The dried solid samples were stored at 22°C for cell wall polysaccharides analysis.

Trifluoroacetic acid hydrolysis and alditol acetate composition analysis

To analyze noncrystalline or amorphous cellulose and other matrix polysaccharides, the dried/washed samples were initially subjected to mild trifluoroacetic acid (TFA) hydrolysis. Here, 250 μl of TFA solution [14.95 ml of 2 M TFA and 1.3 ml of inositol stock solution (5 mg/ml)] was gently added to the walls of each sample tube. Samples were later incubated for 1.5 hours at 121°C on dry bath, and the heating block was then cooled down on ice. The insoluble residue after TFA hydrolysis was pelleted out by centrifuging at 10,000 rpm for 10 min. Next, 25 μl of the solubilized TFA hydrolyzate supernatant was transferred into three separate tubes each without disturbing the solid pellet. Then, 200 μl of isopropyl alcohol (IPA) was added to one of the TFA hydrolyzate glass tubes and dried at 25°C under moderate airflow (~14 kPa) for 35 to 40 min. The resulting small salty pellet was washed with IPA three more times (for a total of four additions) and blow dried at 25°C. The dried tubes were stored inside a dry fridge overnight at 22°C. To the dried TFA hydrolysate, 100 μl of fresh sodium borohydride solution (10 mg of sodium borohydride in 10 ml of 1 M ammonium hydroxide) was added and vortexed at maximum speed. The suspension was incubated at room temperature for 1.5 hours. The sample was neutralized using 150 μl of glacial acetic acid. In the next step, 150 μl of glacial acetic acid and methanol mixture (as a volume ratio, 1:9) was added and evaporated at 35°C under moderate airflow (~14 kPa) for 35 to 40 min. This step was repeated, and the resulting white crystalline residue was resuspended in 250 μl of methanol and evaporated at 35°C twice. To the opaque white residue (dried alditol precipitate), 50 μl of pyridine and 50 μl of acetic anhydride were added and

vortexed thoroughly. Samples were incubated for 20 min at 121°C before cooling the heating blocks on ice. Next, 200 µl of toluene was added and evaporated at 25°C under a gentle airflow (~7 kPa) for 10 to 15 min. The addition of toluene and evaporation step was repeated to obtain a white salty residue. Since the alditol acetate derivatives are volatile, the evaporation processes did not take more than 10 min and were instead stored in a 22°C dry fridge overnight when needed. To the dried alditol acetate derivatives, 1 ml of ethyl acetate (EtOAc) and 1 ml of double-distilled water were added in series and vortexed thoroughly. The phases were separated by centrifuging the tubes at 2000 rpm for 1 min. Last, 1.75 ml of double-distilled water was added to increase the volume for pipetting EtOAc from the top phase, and 200 µl of EtOAc layer was transferred into glass gas chromatography (GC) vials (with glass inserts), and the samples were stored at 4°C overnight or analyzed using GC-MS (Agilent 7890A) directly to estimate the TFA acid hydrolysis released monosaccharides present (as monosaccharide equivalents on dry weight basis of original dried protoplast samples).

Updegraff method for estimating mild acid-resistant crystalline cellulose

To analyze the crystalline cellulose present in regenerated protoplasts analyzed as dried solid samples, 1.5 ml of Updegraff reagent (acetic acid:nitric acid:water = 8:1:2, volume ratio) was added to the TFA hydrolysate and vortexed thoroughly. The samples were heated at 100°C for 30 min, and the solid material was recovered, as detailed in the previous section. The samples were resuspended in 1.5 ml of double-distilled water and 1.5 mL of acetone twice following centrifugation and recovery of cell pellet after each step. Samples were dried at room temperature overnight. Next, 150 µl of 72% sulfuric acid was added to the dried sample and incubated at room temperature for 30 min. After incubation, 875 µl of double-distilled water was added to the samples and vortexed thoroughly. Tubes were centrifuged at 10,000 rpm for 5 min, and the supernatant was collected. Ten microliters of the supernatant was mixed thoroughly with 90 µl of double-distilled water and 200 µl of freshly prepared anthrone solution (2 mg/ml; anthrone in sulfuric acid) in a 96-well plate. The plate was incubated on a plate heater at 80°C for 30 min. The incubated plate was later equilibrated to room temperature for 30 min before measuring the absorbance at 405 nm using a plate reader (Spectramax Plus 384). Samples were compared to the glucose standards, and the error bars are the SDs of the mean. All experiments were performed with at least two replicates.

Enzymatic hydrolysis of protoplast cell walls by cellulases

Fixed protoplasts after cell wall regeneration were used to examine the enzymatic deconstruction in the presence of commercial crude cellulolytic cocktails or purified cellulases. The fixed protoplasts were isolated from the 12% sorbitol and were washed with 25 mM sodium acetate buffer (pH 4.5) twice. The washed protoplasts were incubated with of commercially available cellulase cocktail (1 µg/µl; Cellic CTec2, Novozymes) at room temperature for live imaging of cellulose fibril degradation visualization. See below for the live-cell imaging protocol. The supernatants with released monosaccharides were collected and stored at −20°C for reducing sugars analysis, if needed. Similarly, to examine the selective degradation of cellulose and xyloglucan in the regenerated protoplasts, purified glycosyl hydrolases (E-CELBA from Neogen Corp.) specific toward either cellulose and xyloglucan were used. The fixed protoplasts were incubated at 40°C for 2 hours with the enzymes before imaging. The supernatants were collected and subjected to 3,5-Dinitrosalicylic acid (DNS) reducing sugars assay, as reported previously (*85*).

Preparation of CBM probes for live-cell imaging

It was imperative to use a dye or fluorophore-labeled protein probe in the regeneration media that was stable over extended time durations, had minimal cell toxicity, and did not severely interfere with the growth and assembly of plant cell walls. In addition, the probe had to be highly specific and largely irreversible (i.e., with high association rate but low dissociation rate) in its binding properties to capture even nascent cellulose chains emerging from the plasma membrane. Tandem CBMs or repetitive CBMs exist in nature alongside fungal cellulases and provide high binding specificity to various substrates (*86*). Depending on the type of CBM and the matrix polysaccharide to be imaged, different CBMs have been used as an alternative to classical immunolabeling methods to localize plant cell wall glycans (*87*). CBM3a is widely preferred due to its ability to recognize semicrystalline cellulose in plant cell walls and tissues. Here, we conjugated the Alexa Fluor 568 dye to a tandem CBM3a construct that bound to cellulose. The succinimidyl ester of Alexa Fluor dye is an amine-reactive species and quickly conjugates with the primary amines (of lysine) and amine terminus of proteins. In our previous study, we observed that tandem CBM3a has a higher binding rate than the single CBM3a and could be readily used for real-time imaging of polysaccharides biosynthesis in plants (*57*).

Expression and purification of tandem CBMs was performed as described previously (*57*). pEC-GFP-CBM3a is an *Escherichia coli* expression vector and was provided by the Fox lab (University of Wisconsin–Madison) (*88*). Other CBMs (i.e., CBM17 and CBM1) were prepared as reported elsewhere (*89*). The plasmid was also used as a backbone to insert CBM3a (*Ruminoclostridium thermocellum*) or other CBM genes through the sequence and ligation-independent cloning (*90*, *91*). Sequence-verified plasmid DNA was expressed in *E. coli* BL21-CodonPlus-RIPL [λDE3] and purified using immobilized metal affinity chromatography (IMAC) as mentioned previously (*57*, *92*). For labeling, the tandem CBM3a in phosphate-buffered saline (PBS) buffer was incubated with the fluorophore [Alexa Fluor 568 N-Hydroxysuccinimide (NHS) Ester] at a molar ratio of 1:10 at 4°C and kept in darkness for overnight. The excess fluorophore was removed using gel filtration spin columns (Bio-Rad) according to the manufacturer's specifications. Labeled samples were aliquoted and flash frozen using liquid nitrogen before storing at −80°C.

Confocal microscopy

We fixed the sample with 0.001% glutaraldehyde and added glycine solution (final concentration is 5 mM) as a quenching agent. The fixed protoplasts were incubated in the presence of 200 nM fluorescent dye–labeled tandem CBM3a and washed out the unbound probes with PBS buffer. Second, LM15 antibody was added to the sample at a dilution of 1:20 in PBS buffer. After three washes with PBS buffer, an anti-rat IgG Alexa Fluor secondary antibody was added at a 1:2000 dilution. and the samples were incubated for an additional 1 hour. The samples were stained with CBM probes (or CFW or LM15 antibody) without washing step, and 20 µl of the sample was injected into the sandwich-type chamber assembled with 25-mm round coverslip, GeneFrame (AB0576, Thermo Fisher Scientific) and slide glass (470150-480, VWR International). Confocal imaging was performed with a commercial confocal microscope (Leica TCS

SP8, Leica Microsystems) equipped with a 63×/1.30 glycerin objective lens and two laser lines, 488 and 561 nm. Alexa568 was imaged with a 590- to 615-nm emission bandpass filter under 561-nm excitation, while chloroplast was imaged with a 660- to 690-nm emission bandpass filter under 488-nm excitation. Another confocal microscope (A1, Nikon) was also used to image CFW (excitation: 405 nm/emission: 425 to 475 nm) and chloroplast (excitation: 488 nm/emission: 500 to 550 nm) as shown in fig. S1. The stacked image data were constructed by using ImageJ software (National Institutes of Health) (*93*).

Live plant cell imaging via total internal fluorescence microscopy

We prepared a microwell chamber by attaching a 250-μm holed silicone spacer (MMA-0250-100-08-01, Microsurfaces Pty Ltd.) onto a plasma-cleaned 25-mm coverslip (CS-25R15, Warner Instruments) and inserting the coverslip to a magnetic chamber (Chamlide-CMB, Live Cell Instrument). We filled the chamber with 200 μl of the protoplasts incubation media [60% (v/v) of WI + 40% (v/v) of M2 along with 0.02% BSA and 100 nM of Alexa568-CBM3a probe] in first and then slowly injected 100 μl of protoplast samples into the same media. The samples were usually preincubated for 2 hours to allow the protoplasts to settle to top of the coverslip. For in situ enzymatic reactions, we replaced the sample buffer by gently washing the regenerated protoplast samples with the imaging media (150 nM of Alexa568-CBM3a and 0.02% BSA in pH 5.5 MES buffer) and left the cell wall containing matured cells for 30 min before addition of the enzymes. Before the image acquisition, we lastly add a cellulase, Cellic CTec2 (0.5 mg/ml; Novozymes), and the total volume did not exceed 400 μl.

For the time-lapse imaging to visualize cellulose or cell wall biosynthesis, we use a homebuilt multicolor TIRF (total internal reflection fluorescence) microscope (*94*) with a programmable lamp (Hue lamp, Philips) standing on the upper side of the sample chamber. The lamp is controlled by open-source program (LabVIEW MakerHub, National Instruments) linked to Nikon imaging software (NIS-Elements, Nikon). We set the color of the bulb to warm yellow light: 230 (red), 200 (green), and 100 (blue). In addition, we generated the trigger signal on the NIS-Elements to repetitively switch the lamp off before the acquisition. The images were taken constant rate of 20 s for the drift motion analysis or few minutes for the long-term imaging over several hours. We typically used 2 mW of 561-nm laser excitation along with 580- to 624-nm emission passband (ET605/52m and ZT405/488/561/647/NIR-rpc, Chorma) for observing the cell wall synthesis.

NCC image analysis to quantify cellulose mobility

The NCC matrix ncc($\boldsymbol{A}$, $\boldsymbol{B}$) between matrices $\boldsymbol{A}$ and $\boldsymbol{B}$, representing two images with pixel values A_{ij} and B_{ij}, respectively, is given by

$$\mathrm{ncc}(\boldsymbol{A},\boldsymbol{B}) = \frac{\mathrm{corr}(\boldsymbol{A},\boldsymbol{B})}{\|\boldsymbol{A}\|\,\|\boldsymbol{B}\|}, \quad \text{where} \quad \|\boldsymbol{A}\| = \sum\nolimits_{i,j} A_{ij}^2, \; \|\boldsymbol{B}\| = \sum\nolimits_{i,j} B_{ij}^2$$

and

$$\mathrm{corr}(\boldsymbol{A},\boldsymbol{B}) = \mathscr{Re}\left(\boldsymbol{\mathcal{F}}^{-1}\{\boldsymbol{\mathcal{F}}\{\boldsymbol{A}\}\,\boldsymbol{\mathcal{F}}\{\boldsymbol{B}\}^*\}\right)$$

Here, $\boldsymbol{\mathcal{F}}\{\ \}$ and $\boldsymbol{\mathcal{F}}^{-1}\{\ \}$ represent 2D fast Fourier transform (FFT) and inverse 2D FFT, respectively; $\mathscr{Re}(\ )$ represents the real parts of complex values; and ()* represents complex conjugate operation. ncc($\boldsymbol{A}$, $\boldsymbol{B}$) is a matrix (i.e., 2D grayscale image with pixel values between 0 and 1): its center pixel representing the cross-correlation of $\boldsymbol{A}$ and $\boldsymbol{B}$ without any shift between the two images, and (i,j)th pixel relative to the center representing the cross-correlation calculated with shifting $\boldsymbol{B}$ from $\boldsymbol{A}$ by i columns and j rows. When the two input images have no correlation, all the NCC matrix elements will be nearly zero. When two input images are identical, the NCC matrix will be a 2D bell-shaped curve with the peak value of 1 at the center pixel. If the two input images are identical but one is shifted from the other in the (x, y) plane, then the NCC matrix will be a similar 2D bell-shaped curve with just its peak location displaced from the center pixel by the same image shift amount. Therefore, NCC matrix is commonly used to estimate drift motion with high precision in various microscopy (*95*, *96*).

A fluoresce micrograph typically contains a noise component and also a nonzero, nonuniform background signal, all of which undesirably contribute to NCC. We therefore applied a bandpass filter (*97*) to the input images to remove both the noise and background signals when calculating NCC. We applied NCC to the time-lapse image sequences of fluorescence-labeled cellulose fibrils on protoplast surfaces to quantify the overall cellulose fibrillar motion by the cross-correlation between two consecutive image frames. The cellulose motion between two consecutive image frames largely originates from two sources: first, common drift either due to motion of an entire protoplast cell or microscope instrumental drift; and second, motion of cellulose fibrils themselves on the protoplast surface. These two types of motion will affect the NCC matrix differently. The drift motion will largely shift the peak position, whereas the cellulose motion on the protoplast cell surface will reduce the peak value in the NCC matrix. Therefore, we fitted the NCC matrix with 2D Gaussian functions for a series of two consecutive frames over time and plotted the peak values in time to estimate the drift-corrected overall cellulose fibril motion on the cell surface (e.g., Figs. 3D and 7C).

SMLM of cellulose fibril network

Protoplast cells derived from either wild-type (fig. S7) or prc1-1 transgenic (Fig. 8 and fig. S6) *Arabidopsis* plant lines were incubated in the cell wall regeneration media (WI/M2) for 48 hours until cell surfaces were densely coated with cellulose fibrils. The mature protoplast cells were injected onto the top surface of a coverslip coated with poly-L-lysine (P4707, Sigma-Aldrich). We manually shook the coverslip to carefully peel off the cell wall from the plasma membrane and then removed the media and other debris by pipetting and washing with PBS buffer (pH 7.4). We mounted the coverslip onto a magnetic chamber and stained the sample with Alexa568-CBM3a. For the photoswitching, the PBS buffer was replaced by a fresh imaging buffer mixed with 1× PBS (pH 7.4), glucose oxidase (G2133, Sigma-Aldrich), catalase (C9322, Sigma-Aldrich), Trolox (238813, Sigma-Aldrich), and β-Mercaptoethanol (BME) (63689, Sigma-Aldrich). We acquired 20,000 frames at 33 frames per second through a homebuilt TIRF microscope, and the super-resolution image was reconstructed with custom MATLAB codes. The details of the STORM protocol and data analysis are described elsewhere in the literature (*98*).

Cellulose fibril particle diffusion tracking analysis

We chose several micrometer-sized small fibers from the flat area of the oval-shaped cells and manually tracked each particle using an ImageJ plugin. The speed of drift motion was calculated as the net

movement over total tracking time and averaged all the values. For MSD analysis, data were analyzed with a custom MATLAB code, which extracted the MSD using a function, $<[r(t+\tau) - r(t)]^2>$, for each individual trajectory. The symbol, τ, is time delay. Subdiffusion was analyzed by fitting a linear relation between the log scale of MSD and the log scale of time delay at short time lag (10 frames, i.e., 200 s). We determined the anomalous factor from the slope of fitting parameter and graphed the distribution for 23 distinct fibers (Fig. 4).

Supplementary Materials

The PDF file includes:
Figs. S1 to S9
Legends for movies S1 to S15

Other Supplementary Material for this manuscript includes the following:
Movies S1 to S15

REFERENCES AND NOTES

1. K. Houston, M. R. Tucker, J. Chowdhury, N. Shirley, A. Little, The plant cell wall: A complex and dynamic structure as revealed by the responses of genes under stress conditions. *Front. Plant Sci.* **7**, 984 (2016).
2. D. J. Cosgrove, M. C. Jarvis, Comparative structure and biomechanics of plant primary and secondary cell walls. *Front. Plant Sci.* **3**, 204 (2012).
3. S. Wang, E. Li, I. Porth, J. G. Chen, S. D. Mansfield, C. J. Douglas, Regulation of secondary cell wall biosynthesis by poplar R2R3 MYB transcription factor PtrMYB152 in Arabidopsis. *Sci. Rep.* **4**, 5054 (2014).
4. T. Zhang, Y. Zheng, D. J. Cosgrove, Spatial organization of cellulose microfibrils and matrix polysaccharides in primary plant cell walls as imaged by multichannel atomic force microscopy. *Plant J.* **85**, 179–192 (2016).
5. D. J. Cosgrove, Building an extensible cell wall. *Plant Physiol.* **189**, 1246–1277 (2022).
6. S. Persson, A. Paredez, A. Carroll, H. Palsdottir, M. Doblin, P. Poindexter, N. Khitrov, M. Auer, C. R. Somerville, Genetic evidence for three unique components in primary cell-wall cellulose synthase complexes in Arabidopsis. *Proc. Natl. Acad. Sci. U.S.A.* **104**, 15566–15571 (2007).
7. D. Jayachandran, S. Banerjee, S. P. S. Chundawat, Plant cellulose synthase membrane protein isolation directly from Pichia pastoris protoplasts, liposome reconstitution, and its enzymatic characterization. *Protein Expr. Purif.* **210**, 106309 (2023).
8. B. T. Nixon, K. Mansouri, A. Singh, J. Du, J. K. Davis, J. G. Lee, E. Slabaugh, V. G. Vandavasi, H. O'Neill, E. M. Roberts, A. W. Roberts, Y. G. Yingling, C. H. Haigler, Comparative structural and computational analysis supports eighteen cellulose synthases in the plant cellulose synthesis complex. *Sci. Rep.* **6**, 28696 (2016).
9. P. Purushotham, R. Ho, J. Zimmer, Architecture of a catalytically active homotrimeric plant cellulose synthase complex. *Science* **369**, 1089–1094 (2020).
10. S. Y. Ding, S. Zhao, Y. Zeng, Size, shape, and arrangement of native cellulose fibrils in maize cell walls. *Cellulose* **21**, 863–871 (2014).
11. G. Chinga-Carrasco, Cellulose fibres, nanofibrils and microfibrils: The morphological sequence of MFC components from a plant physiology and fibre technology point of view. *Nanoscale Res. Lett.* **6**, 417 (2011).
12. R. Hooke, *Micrographia: Or, Some Physiological Descriptions of Minute Bodies Made by Magnifying Glasses. With Observations and Inquiries Thereupon* (Printed for J. Allestry, printer to the Royal Society, 1667), pp. 18 p. l., 246, p. 210.
13. M. C. McCann, B. Wells, K. Roberts, Direct visualization of cross-links in the primary plant cell wall. *J. Cell Sci.* **96**, 323–334 (1990).
14. K. Sugimoto, R. E. Williamson, G. O. Wasteneys, New techniques enable comparative analysis of microtubule orientation, wall texture, and growth rate in intact roots of Arabidopsis. *Plant Physiol.* **124**, 1493–1506 (2000).
15. C. I. Lacayo, A. J. Malkin, H. Y. N. Holman, L. Chen, S. Y. Ding, M. S. Hwang, M. P. Thelen, Imaging cell wall architecture in single zinnia elegans tracheary elements. *Plant Physiol.* **154**, 121–133 (2010).
16. S. Y. Ding, Y. S. Liu, Y. Zeng, M. E. Himmel, J. O. Baker, E. A. Bayer, How does plant cell wall nanoscale architecture correlate with enzymatic digestibility? *Science* **338**, 1055–1060 (2012).
17. T. Zhang, S. Mahgsoudy-Louyeh, B. Tittmann, D. J. Cosgrove, Visualization of the nanoscale pattern of recently-deposited cellulose microfibrils and matrix materials in never-dried primary walls of the onion epidermis. *Cellulose* **21**, 853–862 (2014).
18. N. Yilmaz, Y. Kodama, K. Numata, Revealing the architecture of the cell wall in living plant cells by bioimaging and enzymatic degradation. *Biomacromolecules* **21**, 95–103 (2020).
19. A. R. Kirby, A. P. Gunning, K. W. Waldron, V. J. Morris, A. Ng, Visualization of plant cell walls by atomic force microscopy. *Biophys. J.* **70**, 1138–1143 (1996).
20. M. Sauter, R. W. Seagull, H. Kende, Internodal elongation and orientation of cellulose microfibrils and microtubules in deepwater rice. *Planta* **190**, 354–362 (1993).
21. J. P. Verbelen, D. Stickens, In vivo determination of fibril orientation in plant cell walls with polarization CSLM. *J. Microsc.* **177**, 1–6 (1995).
22. C. T. Anderson, A. Carroll, L. Akhmetova, C. Somerville, Real-time imaging of cellulose reorientation during cell wall expansion in Arabidopsis roots. *Plant Physiol.* **152**, 787–796 (2010).
23. J. Liesche, I. Ziomkiewicz, A. Schulz, Super-resolution imaging with Pontamine Fast Scarlet 4BS enables direct visualization of cellulose orientation and cell connection architecture in onion epidermis cells. *BMC Plant Biol.* **13**, 226 (2013).
24. C. H. Haigler, R. M. Brown, M. Benziman, Calcofluor white ST alters the in vivo assembly of cellulose microfibrils. *Science* **210**, 903–906 (1980).
25. M. Benziman, C. H. Haigler, R. M. Brown, A. R. White, K. M. Cooper, Cellulose biogenesis: Polymerization and crystallization are coupled processes in Acetobacter xylinum. *Proc. Natl. Acad. Sci. U.S.A.* **77**, 6678–6682 (1980).
26. I. S. Wallace, C. T. Anderson, Small molecule probes for plant cell wall polysaccharide imaging. *Front. Plant Sci.* **3**, 89 (2012).
27. J. Lehtiö, J. Sugiyama, M. Gustavsson, L. Fransson, M. Linder, T. T. Teeri, The binding specificity and affinity determinants of family 1 and family 3 cellulose binding modules. *Proc. Natl. Acad. Sci. U.S.A.* **100**, 484–489 (2003).
28. K. Ruel, Y. Nishiyama, J. P. Joseleau, Crystalline and amorphous cellulose in the secondary walls of Arabidopsis. *Plant Sci.* **193-194**, 48–61 (2012).
29. D. Mboowa, V. Khatri, J. N. Saddler, The use of fluorescent protein-tagged carbohydrate-binding modules to evaluate the influence of drying on cellulose accessibility and enzymatic hydrolysis. *RSC Adv.* **10**, 27152–27160 (2020).
30. Y. Zheng, X. Wang, Y. Chen, E. Wagner, D. J. Cosgrove, Xyloglucan in the primary cell wall: Assessment by FESEM, selective enzyme digestions and nanogold affinity tags. *Plant J.* **93**, 211–226 (2018).
31. Y. Umemoto, T. Araki, Cell wall regeneration in Bangia atropurpurea (Rhodophyta) protoplasts observed using a mannan-specific carbohydrate-binding module. *Mar. Biotechnol. (NY)* **12**, 24–31 (2010).
32. S. Y. Ding, Q. Xu, M. K. Ali, J. O. Baker, E. A. Bayer, Y. Barak, R. Lamed, J. Sugiyama, G. Rumbles, M. E. Himmel, Versatile derivatives of carbohydrate-binding modules for imaging of complex carbohydrates approaching the molecular level of resolution. *Biotechniques* **41**, 435–443 (2006).
33. D. J. Dagel, Y. S. Liu, L. Zhong, Y. Luo, M. E. Himmel, Q. Xu, Y. Zeng, S. Y. Ding, S. Smith, In situ imaging of single carbohydrate-binding modules on cellulose microfibrils. *J. Phys. Chem. B* **115**, 635–641 (2011).
34. L. Hildén, G. Daniel, G. Johansson, Use of a fluorescence labelled, carbohydrate-binding module from Phanerochaete chrysosporium Ce17D for studying wood cell wall ultrastructure. *Biotechnol. Lett.* **25**, 553–558 (2003).
35. L. McCartney, H. J. Gilbert, D. N. Bolam, A. B. Boraston, J. P. Knox, Glycoside hydrolase carbohydrate-binding modules as molecular probes for the analysis of plant cell wall polymers. *Anal. Biochem.* **326**, 49–54 (2004).
36. S. A. Pfaff, X. Wang, E. R. Wagner, L. A. Wilson, S. N. Kiemle, D. J. Cosgrove, Detecting the orientation of newly-deposited crystalline cellulose with fluorescent CBM3. *Cell Surf.* **8**, 100089 (2022).
37. M. G. L. Gustafsson, Surpassing the lateral resolution limit by a factor of two using structured illumination microscopy. *J. Microsc.* **198**, 82–87 (2000).
38. T. A. Klar, S. Jakobs, M. Dyba, A. Egner, S. W. Hell, Fluorescence microscopy with diffraction resolution barrier broken by stimulated emission. *Proc. Natl. Acad. Sci. U.S.A.* **97**, 8206–8210 (2000).
39. E. Betzig, G. H. Patterson, R. Sougrat, O. W. Lindwasser, S. Olenych, J. S. Bonifacino, M. W. Davidson, J. Lippincott-Schwartz, H. F. Hess, Imaging intracellular fluorescent proteins at nanometer resolution. *Science* **313**, 1642–1645 (2006).
40. M. J. Rust, M. Bates, X. Zhuang, Sub-diffraction-limit imaging by stochastic optical reconstruction microscopy (STORM). *Nat. Methods* **3**, 793–796 (2006).
41. J. Fitzgibbon, K. Bell, E. King, K. Oparka, Super-resolution imaging of plasmodesmata using three-dimensional structured illumination microscopy. *Plant Physiol.* **153**, 1453–1463 (2010).
42. J. Kleine-Vehn, K. Wabnik, A. Martinière, Ł. Łangowski, K. Willig, S. Naramoto, J. Leitner, H. Tanaka, S. Jakobs, S. Robert, C. Luschnig, W. Govaerts, S. W. Hell, J. Runions, J. I. Friml, Recycling, clustering, and endocytosis jointly maintain PIN auxin carrier polarity at the plasma membrane. *Mol. Syst. Biol.* **7**, 540 (2011).
43. B. Dong, X. Yang, S. Zhu, D. C. Bassham, N. Fang, Stochastic optical reconstruction microscopy imaging of microtubule arrays in intact *Arabidopsis thaliana* seedling roots. *Sci. Rep.* **5**, 15694 (2015).
44. K. T. Haas, R. Wightman, E. M. Meyerowitz, A. Peaucelle, Pectin homogalacturonan nanofilament expansion drives morphogenesis in plant epidermal cells. *Science* **367**, 1003–1007 (2020).

45. M. Babi, A. Williams, M. Reid, K. Grandfield, N. D. Bassim, J. M. Moran-Mirabal, Unraveling the supramolecular structure and nanoscale dislocations of bacterial cellulose ribbons using correlative super-resolution light and electron microscopy. *Biomacromolecules* **24**, 258–268 (2023).
46. A. R. Paredez, C. R. Somerville, D. W. Ehrhardt, Visualization of cellulose synthase demonstrates functional association with microtubules. *Science* **312**, 1491–1495 (2006).
47. C. Xiao, T. Zhang, Y. Zheng, D. J. Cosgrove, C. T. Anderson, Xyloglucan deficiency disrupts microtubule stability and cellulose biosynthesis in Arabidopsis, altering cell growth and morphogenesis. *Plant Physiol.* **170**, 234–249 (2015).
48. J. Chan, E. Coen, Interaction between autonomous and microtubule guidance systems controls cellulose synthase trajectories. *Curr. Biol.* **30**, 941–947.e2 (2020).
49. J. Yang, G. Bak, T. Burgin, W. J. Barnes, H. B. Mayes, M. J. Peña, B. R. Urbanowicz, E. Nielsen, Biochemical and genetic analysis identify CSLD3 as a beta-1,4-glucan synthase that functions during plant cell wall synthesis. *Plant Cell* **32**, 1749–1767 (2020).
50. T. Zhang, D. Vavylonis, D. M. Durachko, D. J. Cosgrove, Nanoscale movements of cellulose microfibrils in primary cell walls. *Nat. Plants* **3**, 17056 (2017).
51. H. Kuki, T. Higaki, R. Yokoyama, T. Kuroha, N. Shinohara, S. Hasezawa, K. Nishitani, Quantitative confocal imaging method for analyzing cellulose dynamics during cell wall regeneration in Arabidopsis mesophyll protoplasts. *Plant Direct* **1**, e00021 (2017).
52. S. Tagawa, Y. Yamagishi, U. Watanabe, R. Funada, T. Kondo, Dynamics of structural polysaccharides deposition on the plasma-membrane surface of plant protoplasts during cell wall regeneration. *J. Wood Sci.* **65**, 47 (2019).
53. H. Kuki, R. Yokoyama, T. Kuroha, K. Nishitani, Xyloglucan is not essential for the formation and integrity of the cellulose network in the primary cell wall regenerated from *Arabidopsis* protoplasts. *Plants (Basel)* **9**, 629 (2020).
54. K. Sakai, F. Charlot, T. L. Saux, S. Bonhomme, F. Nogué, J. C. Palauqui, J. Fattaccioli, Design of a comprehensive microfluidic and microscopic toolbox for the ultra-wide spatio-temporal study of plant protoplasts development and physiology. *Plant Methods* **15**, 79 (2019).
55. R. Dixit, R. Cyr, Cell damage and reactive oxygen species production induced by fluorescence microscopy: Effect on mitosis and guidelines for non-invasive fluorescence microscopy. *Plant J.* **36**, 280–290 (2003).
56. J. Icha, M. Weber, J. C. Waters, C. Norden, Phototoxicity in live fluorescence microscopy, and how to avoid it. *Bioessays* **39**, 1700003 (2017).
57. D. Jayachandran, P. Smith, M. Irfan, J. Sun, J. M. Yarborough, Y. J. Bomble, E. Lam, S. P. S. Chundawat, C. P. S. S. Chundawat, Engineering and characterization of carbohydrate-binding modules for imaging cellulose fibrils biosynthesis in plant protoplasts. *Biotechnol. Bioeng.* **120**, 2253–2268 (2023).
58. N. Uppugundla, L. Da Costa Sousa, S. P. S. Chundawat, X. Yu, B. Simmons, S. Singh, X. Gao, R. Kumar, C. E. Wyman, B. E. Dale, V. Balan, A comparative study of ethanol production using dilute acid, ionic liquid and AFEX™ pretreated corn stover. *Biotechnol. Biofuels* **7**, 72 (2014).
59. M. C. Hernandez-Gomez, M. G. Rydahl, A. Rogowski, C. Morland, A. Cartmell, L. Crouch, A. Labourel, C. M. G. A. Fontes, W. G. T. Willats, H. J. Gilbert, J. P. Knox, Recognition of xyloglucan by the crystalline cellulose-binding site of a family 3a carbohydrate-binding module. *FEBS Lett.* **589**, 2297–2303 (2015).
60. M. G. Rydahl, A. R. Hansen, S. K. Kračun, J. Mravec, Report on the current inventory of the toolbox for plant cell wall analysis: Proteinaceous and small molecular probes. *Front. Plant Sci.* **9**, 349879 (2018).
61. L. Colin, R. Martin-Arevalillo, S. Bovio, A. Bauer, T. Vernoux, M. C. Caillaud, B. Landrein, Y. Jaillais, Imaging the living plant cell: From probes to quantification. *Plant Cell* **34**, 247–272 (2022).
62. D. M. Cavalier, O. Lerouxel, L. Neumetzler, K. Yamauchi, A. Reinecke, G. Freshour, O. A. Zabotina, M. G. Hahn, I. Burgert, M. Pauly, N. V. Raikhel, K. Keegstra, Disrupting two Arabidopsis thaliana xylosyltransferase genes results in plants deficient in xyloglucan, a major primary cell wall component. *Plant Cell* **20**, 1519–1537 (2008).
63. T. N. M. Van Amstel, H. M. P. Kengen, Callose deposition in the primary wall of suspension cells and regenerating protoplasts, and its relationship to patterned cellulose synthesis. *Can. J. Bot.* **74**, 1040–1049 (1996).
64. R. H. Abou-Saleh, M. C. Hernandez-Gomez, S. Amsbury, C. Paniagua, M. Bourdon, S. Miyashima, Y. Helariutta, M. Fuller, T. Budtova, S. D. Connell, M. E. Ries, Y. Benitez-Alfonso, Interactions between callose and cellulose revealed through the analysis of biopolymer mixtures. *Nat. Commun.* **9**, 4538 (2018).
65. K. J. D. Lee, S. E. Marcus, J. P. Knox, Cell wall biology: Perspectives from cell wall imaging. *Mol. Plant.* **4**, 212–219 (2011).
66. J. Auernhammer, M. Langhans, J.-L. Schäfer, T. Keil, T. Meckel, M. Biesalski, R. W. Stark, Nanomechanical subsurface characterisation of cellulosic fibres. *SN Appl. Sci.* **4**, 160 (2022).
67. M. Linder, M. L. L. Mattinen, M. Kontteli, G. Lindeberg, J. Ståhlberg, T. Drakenberg, T. Reinikainen, G. Pettersson, A. Annila, Identification of functionally important amino acids in the cellulose-binding domain of Trichoderma reesei cellobiohydrolase I. *Protein Sci.* **4**, 1056–1064 (1995).
68. M. Linder, T. T. Teeri, The cellulose-binding domain of the major cellobiohydrolase of Trichoderma reesei exhibits true reversibility and a high exchange rate on crystalline cellulose. *Proc. Natl. Acad. Sci. U.S.A.* **93**, 12251–12255 (1996).
69. J. M. Fox, P. Jess, R. B. Jambusaria, G. M. Moo, J. Liphardt, D. S. Clark, H. W. Blanch, A single-molecule analysis reveals morphological targets for cellulase synergy. *Nat. Chem. Biol.* **9**, 356–361 (2013).
70. R. S. Atalla, M. F. Crowley, M. E. Himmel, R. H. Atalla, Irreversible transformations of native celluloses, upon exposure to elevated temperatures. *Carbohydr. Polym.* **100**, 2–8 (2014).
71. Y. Zhang, J. Yu, X. Wang, D. M. Durachko, S. Zhang, D. J. Cosgrove, Molecular insights into the complex mechanics of plant epidermal cell walls. *Science* **372**, 607–711 (2021).
72. F. Huang, G. Sirinakis, E. S. Allgeyer, L. K. Schroeder, W. C. Duim, E. B. Kromann, T. Phan, F. E. Rivera-Molina, J. R. Myers, I. Irnov, M. Lessard, Y. Zhang, M. A. Handel, C. Jacobs-Wagner, C. P. Lusk, J. E. Rothman, D. Toomre, M. J. Booth, J. Bewersdorf, Ultra-high resolution 3D imaging of whole cells. *Cell* **166**, 1028–1040 (2016).
73. S. Liu, H. Huh, S. H. Lee, F. Huang, Three-dimensional single-molecule localization microscopy in whole-cell and tissue specimens. *Annu. Rev. Biomed. Eng.* **22**, 155–184 (2020).
74. J. Tormo, R. Lamed, A. J. Chirino, E. Morag, E. A. Bayer, Y. Shoham, T. A. Steitz, Crystal structure of a bacterial family-III cellulose-binding domain: A general mechanism for attachment to cellulose. *EMBO J.* **15**, 5739–5751 (1996).
75. P. Albersheim, A. Darvill, K. Roberts, R. Sederoff, A. Staehelin, *Plant Cell Walls* (CRC Press, 2010), p. 430.
76. Y. Nishiyama, Molecular interactions in nanocellulose assembly. *Philos. Trans. A. Math. Phys. Eng. Sci.* **376**, 20170047 (2018).
77. P. Chen, Y. Nishiyama, J. Wohlert, Quantifying the influence of dispersion interactions on the elastic properties of crystalline cellulose. *Cellulose* **28**, 10777–10786 (2021).
78. M. Wohlert, T. Benselfelt, L. Wågberg, I. Furó, L. A. Berglund, J. Wohlert, Cellulose and the role of hydrogen bonds: Not in charge of everything. *Cellulose* **29**, 1–23 (2022).
79. Y. B. Park, D. J. Cosgrove, A revised architecture of primary cell walls based on biomechanical changes induced by substrate-specific endoglucanases. *Plant Physiol.* **158**, 1933–1943 (2012).
80. L. Yu, Y. Yoshimi, R. Cresswell, R. Wightman, J. J. Lyczakowski, L. F. L. Wilson, K. Ishida, K. Stott, X. Yu, S. Charalambous, J. Wurman-Rodrich, O. M. Terrett, S. P. Brown, R. Dupree, H. Temple, K. Krogh, P. Dupree, Eudicot primary cell wall glucomannan is related in synthesis, structure, and function to xyloglucan. *Plant Cell* **34**, 4600–4622 (2022).
81. J. Sheen, Signal transduction in maize and Arabidopsis mesophyll protoplasts. *Plant Physiol.* **127**, 1466–1475 (2001).
82. S. D. Yoo, Y. H. Cho, J. Sheen, Arabidopsis mesophyll protoplasts: A versatile cell system for transient gene expression analysis. *Nat. Protoc.* **2**, 1565–1572 (2007).
83. J. H. M.Willison, A. S.Klein, "Cell-wall regeneration by protoplasts isolated from higher plants" in *Cellulose and Other Natural Polymer Systems* (Springer, 1982), pp. 61–85.
84. T. Engelsdorf, N. Gigli-Bisceglia, M. Veerabagu, J. F. McKenna, L. Vaahtera, F. Augstein, D. Van der Does, C. Zipfel, T. Hamann, The plant cell wall integrity maintenance and immune signaling systems cooperate to control stress responses in Arabidopsis thaliana. *Sci. Signal.* **11**, 3070 (2018).
85. Y. Liu, B. Nemmaru, S. P. S. Chundawat, Thermobifida fusca cellulases exhibit increased endo-exo synergistic activity, but lower exocellulase activity, on cellulose-III. *ACS Sustain. Chem. Eng.* **8**, 5028–5039 (2020).
86. M. S. Møller, S. E. Bouaballati, B. Henrissat, B. Svensson, Functional diversity of three tandem C-terminal carbohydrate-binding modules of a β-mannanase. *J. Biol. Chem.* **296**, 100638 (2021).
87. A. W. Blake, L. McCartney, J. E. Flint, D. N. Bolam, A. B. Boraston, H. J. Gilbert, J. P. Knox, Understanding the biological rationale for the diversity of cellulose-directed carbohydrate-binding modules in prokaryotic enzymes. *J. Biol. Chem.* **281**, 29321–29329 (2006).
88. T. A. Whitehead, C. K. Bandi, M. Berger, J. Park, S. P. S. Chundawat, Negatively supercharging cellulases render them lignin-resistant. *ACS Sustain. Chem. Eng.* **5**, 6247–6252 (2017).
89. S. P. S. Chundawat, B. Nemmaru, M. Hackl, S. K. Brady, M. A. Hilton, M. M. Johnson, S. Chang, M. J. Lang, H. Huh, S. H. Lee, J. M. Yarbrough, C. A. López, S. Gnanakaran, Molecular origins of reduced activity and binding commitment of processive cellulases and associated carbohydrate-binding proteins to cellulose III. *J. Biol. Chem.* **296**, 100431 (2021).
90. J. Stevenson, J. R. Krycer, L. Phan, A. J. Brown, A practical comparison of ligation-independent cloning techniques. *PLOS ONE* **8**, 8–14 (2013).
91. J. A. Walker, T. E. Takasuka, K. Deng, C. M. Bianchetti, H. S. Udell, B. M. Prom, H. Kim, P. D. Adams, T. R. Northen, B. G. Fox, Multifunctional cellulase catalysis targeted by fusion to different carbohydrate-binding modules. *Biotechnol. Biofuels.* **8**, 220 (2015).
92. B. Nemmaru, N. Ramirez, C. J. Farino, J. M. Yarbrough, N. Kravchenko, S. P. S. Chundawat, Reduced type-A carbohydrate-binding module interactions to cellulose I leads to improved endocellulase activity. *Biotechnol. Bioeng.* **118**, 1141–1151 (2021).

93. C. A. Schneider, W. S. Rasband, K. W. Eliceiri, NIH Image to ImageJ: 25 years of image analysis. *Nat. Methods* **9**, 671–675 (2012).
94. S.-H. Lee, Optimal integration of wide field illumination and holographic optical tweezers for multimodal microscopy with ultimate flexibility and versatility. *Opt. Express* **26**, 8049–8058 (2018).
95. X. Li, P. Mooney, S. Zheng, C. R. Booth, M. B. Braunfeld, S. Gubbens, D. A. Agard, Y. Cheng, Electron counting and beam-induced motion correction enable near-atomic-resolution single-particle cryo-EM. *Nat. Methods* **10**, 584–590 (2013).
96. Y. Wang, J. Schnitzbauer, Z. Hu, X. Li, Y. Cheng, Z.-L. Huang, B. Huang, Localization events-based sample drift correction for localization microscopy with redundant cross-correlation algorithm. *Optic. Express* **22**, 15982–15991 (2014).
97. J. C. Crocker, D. G. Grier, Methods of digital video microscopy for colloidal studies. *J. Colloid Interface Sci.* **179**, 298–310 (1996).
98. S. Atwal, J. Wongsantichon, S. Giengkam, K. Saharat, Y. J. Pittayasathornthun, S. Chuenklin, L. C. Wang, T. Chung, H. Huh, S. H. Lee, R. M. Sobota, J. Salje, The obligate intracellular bacterium Orientia tsutsugamushi differentiates into a developmentally distinct extracellular state. *Nat. Commun.* **13**, 3603 (2022).

Acknowledgments: We thank S. Burley (Rutgers University) and K. Keegstra (Michigan State University) for providing helpful comments on the manuscript. We thank R. Johnson and L. Alexander from the GLBRC biomass analytical facility for conducting the composition analysis on protoplast samples. **Funding:** This work was primarily supported by the Department of Energy (DOE) award DE-SC0019313. S.-H.L. and S.P.S.C. also acknowledge partial support from the Rutgers Office of Research and Innovation. S.P.S.C. acknowledges partial support from his NSF CBET Career Award (1846797). S.-H.L. acknowledges partial support from Rutgers New Faculty Startup Fund through the Institute for Quantitative Biomedicine. The GLBRC core facility work is supported in part by the Great Lakes Bioenergy Research Center, US Department of Energy, Office of Science, Office of Biological and Environmental Research under award number DE-SC0018409. **Author contributions:** S.P.S.C., E.L., and S.-H.L. conceived and supervised the study. H.H. led and conducted all the imaging experiments including SEM, confocal, TIRFM, and STORM microscopy work. D.J. developed, characterized, and produced all CBM-based dyes used for imaging. D.J. led all biochemical and cell wall composition experiments and data analysis. H.H., M.I., D.J., and J.S. developed and validated the plant protoplast cell wall regeneration assay. J.S. maintained the *Arabidopsis* plants and generated protoplasts for the team. H.H. and S.-H.L. analyzed all the microscopy data. D.J., with the assistance of H.H., prepared an initial incomplete manuscript draft along with critical inputs from S.P.S.C., E.L., and S.-H.L. prepared the final figures/movies and wrote the final complete version of paper. All the authors reviewed, edited, and approved of the final manuscript draft. **Competing interests:** The authors declare that they have no competing interests. **Data and materials availability:** All data needed to evaluate the conclusions in the paper are present in the paper and/or the Supplementary Materials.

Submitted 26 August 2024
Accepted 14 February 2025
Published 21 March 2025
10.1126/sciadv.ads6312